Carboniferous–Permian transgression/regression mechanisms in the Eastern Ordos Basin and their sea-level spatiotemporal variability: Insights from source-to-sink systems

Chao Fu, Xinghe Yu, Shunli Li, Zixiao Peng, Shi Shi

Journal Pre-proof

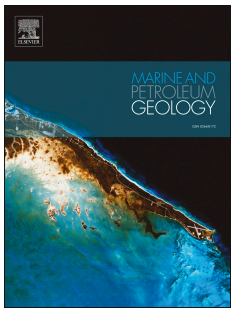

Carboniferous–Permian transgression/regression mechanisms in the Eastern Ordos Basin and their sea-level spatiotemporal variability: Insights from source-to-sink systems

Chao Fu, Xinghe Yu, Shunli Li, Zixiao Peng, Shi Shi

PII: S0264-8172(20)30505-5

DOI: https://doi.org/10.1016/j.marpetgeo.2020.104722

Reference: JMPG 104722

To appear in: *Marine and Petroleum Geology*

Received Date: 12 May 2020

Revised Date: 16 September 2020

Accepted Date: 19 September 2020

Please cite this article as: Fu, C., Yu, X., Li, S., Peng, Z., Shi, S., Carboniferous–Permian transgression/regression mechanisms in the Eastern Ordos Basin and their sea-level spatiotemporal variability: Insights from source-to-sink systems, *Marine and Petroleum Geology* (2020), doi: https://doi.org/10.1016/j.marpetgeo.2020.104722.

Chao FU: Writing- Original draft preparation

Xinghe YU: Supervision.

Shunli LI: Visualization, Investigation.

Zixiao PENG: Software, Validation.

Shi SHI: Software

Carboniferous–Permian transgression/regression mechanisms in the Eastern Ordos Basin and their sea-level spatiotemporal variability: Insights from source-to-sink systems

Chao Fu[1,2] , Xinghe Yu[1], Shunli Li[1], Zixiao Peng[1], Shi Shi[3]*

1 School of Energy, China University of Geosciences, Beijing 100083, China

2 Rennes Geosciences, Université de Rennes 1, Rennes 35000, France

3 Coalbed methane company, China National Petroleum Corporation, Beijing 100020 China

corresponding author: billyu@cugb.edu.cn

Abstract: Developed on the North China Craton, the intracratonic Ordos Basin contains a complete Paleozoic-to-Cenozoic sediment record, allowing for long-term paleoenvironmental and climate change investigation. During the Carboniferous–Permian period, convergence between the North China block and the paleo-Yangtze plate to the south resulted in a general marine regression characterized by a series of second-order transgression/regression cycles diachronous along the eastern margin of the Ordos. However, the detailed mechanisms that induced these cycles, as well as the associated paleoecological changes, remain unknown. In this study, we integrate multiple indices, including δ18O and δ13C, rare earth element (REE), paleontological assemblages, and clay content (*w* (chlorite + kaolinite)/*w*((Illite) ratio) planar distribution, to restore the paleo-water depth distribution. These parameters are then used to reconstruct the paleo-sea level from the Pennsylvanian to the middle Permian. We conclude that the direction of second-order transgression/regression was mainly toward the east during the Pennsylvanian–early Permian and switched clockwise toward the north during the middle Permian. We suggest that the second-order cycles, diachronous in space and time, are mainly

linked to local variations in sediment supply and regional uplift. Using detrital zircon U–Pb data and the REE and trace element content and heavy mineral assemblages (HMA), we estimate the sediment provenance area. The sediment volumes deposited in the basin through time are obtained using 2D seismic data. During the Carboniferous, the coarse-grained sediments deposited in the eastern Ordos were derived from the uplifting Helan Mountain (Qiandam–Qilian orogenic belt). By the middle Permian, the detrital material became multi-sourced, thus issuing the Yinshan range to the north and the Qinling range to the south. We then integrate the description of numerous core samples with electric log and 2D seismic data to reconstruct the sediment facies associations across the first-order regression from the Carboniferous tidal flat depositional system to the middle Permian prograding fluvial delta system. According to the transfer of the glacial epoch, the sedimentation rate, and the transgression/regression rate above, we classify the evolution process into three patterns: low-transgression rate and less-sediment supply pattern (the late Carboniferous), high regression rate and mass sediment supply pattern (the north block during the early Permian), and low regression rate and mass sediment supply pattern (the south block during the Sakmarian stage). Lastly, with the quantitative calculation of the source-to-sink (S2S) parameters, including the S2S system volume and the elevated height of regional uplift with the 2D seismic data, we propose the mechanism of transgression/ regression in the Ordos Basin, responding to the above three pattern s. The first pattern was controlled by regional uplift, whereas the second pattern was controlled by sediment supply. As to the third one, uplift and sediment supply could affect the transgression/regression process.

Keywords : Transgression mechanism, Provenance identification, Detrital geochronology data, Paleontology data, Pennsylvanian–Permian transition

1. Introduction

An intracratonic basins is characterized by the preponderance of thermal subsidence over tectonic subsidence, making for largely stable long-term subsidence rates. Sedimentary sequences in this type of basin generally preserve a complete sedimentary record that allows deciphering the large-scale paleoenvironmental evolution (*Sloss, 1963; McLaughlin et al., 2004; Zhu et al., 2008; Hoffmann et al., 2009*). When affected by marine incursions, these basins provide a good record of water-depth fluctuations and associated transgression/regression mechanisms (*Nikishin et al., 1996; Martins-Neto et al., 2001; Alkmim and Martins-Neto, 2012; Bumby et al., 2012*). As a typical intracratonic basin in the western part of the North China Block, the Ordos Basin (*Wang et al., 2019; Yin et al., 2019; Shi et al., 2020*) contains a complete Carboniferous–Permian sedimentary record of transgression/regression cycles closely related in time to a transition from a glacial period to an interglacial one (*Tabor and Poulsen, 2008; Koch and Frank, 2011; Xu et al., 2020*).

Previous studies have pointed out that with the end of the Late Paleozoic Ice Age (LPIA) during the late Permian, the increase in rainfall resulted in additional sediment supply worldwide, leading to a marine regression process in shallow-marine basins (*Golonka and Ford, 2000; Tabor and Poulsen, 2008; Koch and Frank, 2011*). However, *Stollhofen et al.,* (*2000*) pointed out that the transgression/regression process shows a spatiotemporal variability within the large study area. Using stable isotope analysis ($\delta^{13}C$ and $\delta^{15}N$) in the eastern margin area (EMA) of the Ordos Basin, *Xu et al. (2020)* further highlighted the complexity of the transgression/regression events. Meanwhile, *Zhu et al. (2008) and Zhang et al. (1997*) suggested that during the Carboniferous–Permian, the water depth in the EMA continuously declined due to uplift of the

basin margins (***FIG. 1***). Finally, Jiang and Wang (2012) demonstrated that the main direction of the transgression/regression phases changed constantly through time, adding complexity to the water-depth fluctuation pattern.

Several authors have suggested that tectonic movements linked to continental accretions along the margins of the North China Craton had been the main driving mechanism of water depth changes in the basin (*Qin et al., 2002; Yang et al., 2005*). However, by focusing their models on the effects of tectonics, these studies neglected the influence of changes in climate and sediment supply rates, which are also factors of water-depth fluctuation, particularly in shallow, marginal basins *(Haq et al., 1987; Haq and Schutter, 2008a; Labaune et al., 2008; De Falco et al., 2015; Fu et al., 2019*). Indeed, existing studies have shown that on the eastern margin of the Ordos Basin, the direction of the main sediment supply changed during the Carboniferous–Permian period, implying changes in regional topography and erosion pattern (*Kröner et al., 2006; Darby and Gehrels, 2006; Milne et al. 2009; Zhu et al., 2011*). Regarding intracratonic basins, *Klein (1982)* suggested that an arid climate can potentially change the ratio between clastic and carbonate deposits and indirectly affect water depth.

In this study, we point out the water-depth variations and derive local and regional transgression/regression cycles for the Pennsylvanian-to-early-Permian period. We then integrate detrital zircon U-Pb analysis, heavy mineral assemblages (HMA), and trace elements indexes to determine major changes in sediment sources, climate, transport conditions, and depositional environments. We then quantitatively compare the sediment composition and supply rates to water-depth fluctuations and propose three major source-to-sink (S2S) patterns for the late Paleozoic eastern Ordos Basin: low-transgression rate and limited sediment supply (LT–LS),

low-transgression rate and massive sediment supply (LT–MS), and high-transgression rate and massive sediment supply (HT–MS). Finally, the response to these various patterns in terms of water-depth variations is described to document the transgression/regression cycles during the final stage of the LPIA.

2.Geological Setting

The Mesozoic-to-Cenozoic geologic history of Central China has been strongly influenced by continental accretion events along the southern margin of the Eurasian continent. These geodynamic events drove the formation and sometimes the reactivation of mountain ranges such as the Lvliang and Helen-Liupan Mountains east and west of the Ordos Basin, the Yinshan Mountain to the north and the Qinling Mountain to the south (***FIG. 1***). The Ordos Basin itself is formed by several depressions such as the East margin, Hetao, Weihe, and Yichuan depressions while major faults control the basin boundaries. The evolution of the Ordos Basin can be divided into five main stages: it initiated as a Cambrian–Early Ordovician continental rim basin, evolving towards an intracratonic basin in a Middle Ordovician–Middle Triassic generally compressive geodynamic setting; during the Late Triassic–Early Cretaceous the basin was affected by thermal subsidence before being inverted and eroded during the late Cretaceous to Neogene compressive event (only some Cenozoic loess are preserved in the south part the basin (*Yuan et al., 2007*)).

The sedimentary sequence preserved in the EMA ranges from 7 km to 10 km in thickness (*Yang et al., 2005*). During the Ordovician to Mississipian period, tectonic activity induced uplift of the eastern margin of the Ordos Basin (present-day reference frame) leading to a regional parallel unconformity between the basement and the Pennsylvanian deposits (*Yang et al., 2005*).

The Pennsylvanian to Permian series are divided into the following formations: Penci (C_2b), Taiyuan (C_2t), Shanxi (P_1s itself divided into the upper and lower P_1s members), Lower Shihotse (P_2sh), Upper Shihotse (P_3sh), and Shiqianfeng (P_3s) (***FIG.2***).

During the deposition of the Penci Formation (Fm.), the sedimentary record displays a sharp regression phase generally associated to the uplift of the central part of the Ordos region. The facies association evolves from a shallow marine setting to a coastal swamp environment. Based on core sample interpretation, *Zhang et al. (1997) and Jiang and Wang (2012)* indicated that alluvial fan or braided delta depositional environments dominated in the northern part of the study area. *Stanley and Powell (2003*) stated that in the late Pennsylvanian period, the arid climate and the correlatively reduced amount of sediment injected into the basin resulted in the development of thick limestone and coal seams in the Taiyuan Fm. However, the sea level showed a gentle transgression, and a carbonate platform dominated during this period.

In the early Permian, the convergence between the South China and North China plates largely modified the paleomorphology and paleoecology of the Ordos region. Furthermore, the increasing sediment supply from multiple directions led to a gentle regression from the Asselian to the Kungerian stages (Shanxi Fm.). The combined studies of *Zhang et al. (1997), Zhu et al. (2008), and Xin et al. (2018)* pointed out that deltaic environments dominated in the EMA, with large marshes separating the distributary channels. With the decrease in sea level, the meandering channels in the delta plains were replaced by braided river environments marked by sand bars and crevasse splays.

3.Data and methodology

3.1 Research data

The EMA of the Ordos Basin has been explored by 3700 km of 2D seismic and 1000 km^2 of 3D high-resolution seismic data. Furthermore, we get access to 15 wells drilled in the EMA. The positions of the cross-well seismic sections used in this study are shown in ***FIG. 1a.*** Electric well-log data, including gamma ray (GR), were acquired and processed by Schlumberger®. We get the core samples from wells DJ12, Y253, DJ43, G10, G6, and DJ19 (***FIG. 3***). Heavy and clay mineral content and their scanning electron microscope (SEM) photographs as well as whole rock trace elements analysis from wells H4, Y787, G3, DJ43, DJ53, Y521, Y653, and Y432 were processed by the Geological Laboratory of the Research Institute of C.M.B. company (China National Petroleum Corporation CNPC®). The paleontological identifications, including pollen and plant assemblages from wells G3, H4, DJ43, DJ53, and Y787, were completed by the Langfang Branch of Petrochina Exploration and Development Research Institute (CNPC®).

LA-ICP-MS U–Pb analysis of detrital zircons from four core samples (DJ53 1942.23 m, H5 1968.1 m, DJ51 2264.85 m, and G2 2048.1 m) was completed by the Chinese Academy of Geological Sciences® (***Appendix TABLES 1–4***). Laser ablation was conducted using a NWR193UC 193 nm deep ultraviolet laser ablation sampling system (Elemental Scientific Lasers, USA). Mass spectrometry was calculated using an Agilent 7900 inductively coupled plasma mass spectrometer (Agilent, USA). One hundred twenty detrital zircons from each sample were analyzed with a spot size of 30 μm. Every five analyses were followed by one analysis of standard zircon 91500 and GJ. Common lead correction was conducted using ComPbCorr#3_15G. The U–Pb age calculations and Concordia diagram were completed using *IsoplotR*® software provided by University College London, UK (http://pieter-vermeesch.es.ucl.ac.uk/shiny/IsoplotR/). Only zircon ages concordant within 90%–110% were

considered in the subsequent discussion.

$\delta^{18}O$ and $\delta^{13}C$ data were analyzed from whole-sediment mudstone, limestone, or coal samples from cores Y787, DJ53, DJ43, H4, and G4 (some carbonate poor layers did not provide reliable data and results were not reported). The C and O-isotope analyses results are normalized to the Pee Dee Belemnite (PDB) standards with a precision of ±0.1‰ for $\delta^{13}C$ and ±0.2‰ for $\delta^{18}O$.

3.2 Methodology

1) Sedimentology and stratigraphy analysis from drill cores and seismic data

Facies association were established from core samples according to the sedimentary structure (***FIG.3***) and the grain-size distribution (***FIG.4***). Geophysical log data were then used to constrain the depositional environment setting, such as the bell or cylinder shape of the GR curve (indicating a decreasing flow rate), or a sharp decrease of the DEN curve (or sonic/neutron porosity curve) indicating the occurrence of coal. Finally, associating well and 2D seismic data we reconstructed the stratigraphic and depositional environment pattern of the EMA of the Ordos Basin through time. The 2D seismic profiles were studied and interpreted following the methodology previously established by *Pu et al. (2009), Xu et al. (2016),* and *Anees et al. (2019)* in the Ordos Basin. Three types of seismic facies were used as guidelines: the concave, convex, and plate shapes. Following that approach, a seismic package with a concave boundary was generally interpreted as an eroding channel. Associating the log data to the seismic image, it was possible to distinguish between deposited tidal channels, braided channel belts and depositional meandering channel belts. Convex-shaped seismic facies were generally interpreted as depositional tidal barriers. The plate-shaped seismic facies, characterized by a high amplitude

seismic reflection, generally indicate the development of carbonated tidal platforms.

2) Identification of sediment provenance area and calculation of supply rates.

By combining the results of previous studies constraining the provenance area of the EMA during the late Paleozoic (*Darby and Gehrels, 2006; Kröner et al., 2006; Zhu et al., 2011; Song et al., 2012; Xie and Heller, 2013; Sun et al., 2014*), we established a mean zircon U–Pb age distribution for the EMA. Using both the age data for the basement rocks, the zircon–tourmaline–rutile (ZTR) index (provides indications on the distance of sediment transportation), grains size, sediments Rare Earth Elements patterns and informations on the tectonic background *(Darby and Gehrels, 2006; Xie and Heller, 2013*), we evaluated the evolution of the main provenance area during the interval from Pennsylvanian to the early Permian.

The sediment supply rates through time were calculated using the provenance data obtained from the method described above and a series of selected 2D seismic profiles. The thickness of the main sediment layers (A parameter hereafter) corresponding to the Bashkirian to Sakmarian stages was obtained from seismic data. As shale deposits have a much higher compaction coefficient then sandstone layers we divided the strata using the sand content (over 80%) observed within the corresponding reference wells (*Yang et al., 2008; Zhang et al., 2009; Zou et al., 2013*). Pre-compaction thicknesses were then calculated using compaction coefficients of 0.0004 m^{-1} for mudstone and 0.00025 m^{-1} for sandstone (*Zhang et al., 2009*). Finally, the stratigraphic and geochronology data obtained in reference wells were used as time constrains (T) to derive sedimentation rates ($v_{sediment}$= A/T).

3) Regional paleo-sea level reconstruction via multi-index integration

As sea level fluctuates all the time, the lateral facies variations observed in the sedimentary

record may lead to some illusion and contradiction in the reconstructed regional paleo-sea level. In this study we computed the relative sea level of the Ordos Basin EMA based on the $\delta^{18}O$ and $\delta^{13}C$ data from the high organic matters mudstone and comparing to the similar curve obtained by Xin et al. (2018). Our interpretation takes tinto account the fact that the warming climate during the Carboniferous–Permian transgression accounted for an increase of 0.008–0.01‰m^{-1} of the $\delta^{18}O_{(V\text{-}PDB)}$ value (*Adkins et al., 2002; Elderfield et al., 2012*).

A second independent model was derived from paleontological data. *Paripters spp.–Linopteris spp.–Conchophyllum* plant association are characteristic of the Bashkirian–Kasimovian stage. During the Gzhelian–Asselian stage, the representative paleontological assemblage is composed of *Neurpteris pseudovata* and *Lepidodendron posthumii.* Then, with the warming climate, *Emplectopteridium alatum–Cathaysiopteris whitei–Emplectopteris triangularis* occurred during the Sakmarian–Kungurian stage (*Hilton and Cleal, 2007*). Some species (*Zygopteris* and *Ankyropteris corrugated)* accumulation, including their macro-remains and pollen, reflected an onshore setting *(Phillips and Galtier, 2005; Phillips and Galtier, 2011*). Hence, we calculated the ratio of fern species biomass and the plant fossil identified($w_{biomass}$) in G3, H4, DJ43, DJ53, and Y787 and obtain their responding relative sea level. Furthermore, according to the morphology of all the identified species in the core samples of the EMA (*Hilton and Cleal, 2007; Pfefferkorn and Wang, 2007*), broadleaf ferns were prominent during the late Paleozoic although their preservation in the fossil record was affected by post-deposition sediment reworking processes (*Bacon et al., 2016*). Previous studies have pointed out that at the high stand of the sea level, the amount of leaf fossil in the core samples (w_{leaf}) is larger than the root or steam fossil due to the hydrodynamic process of tide or wave (*Pratt et al., 1978; Gastaldo, 2004; Gee, 2005*). Thus, according to the ratio

between the leaf fossil and the root/ steam fossil (w_{leaf}), we can infer the relative sea level.

Clay mineral assemblages provide another evidence for the late Paleozoic relative regional sea-level proxy. The Panthalassic ocean margin was located east of the EMA and south of the Paleo–Tethys (*http://www.scotese.com/*). The clay mineral assemblages of the Panthalassic ocean (*Kemp and Izumi, 2014*) and Paleo–Tethys *(Cheng et al., 2019*) display a high value of illite. By contrast, the clay mineral assemblage of the potential source area is mainly chlorite and kaolinite (*Zhang et al., 1998*). Thus, the deposition of the marine original sediment will lead to a gentle increase of the illite content in the sediment. That is to say, the illite shows a much weaker positive relationship to the transgression process. According to the method mentioned in *Fu et al. (2019a and b)*, we calculated the w_{clay}=*w*(chlorite + kaolinite)/*w*((illite), and variations in this parameter are inversely correlated to the variations in sea-level.

The trace element ratios including ΣLREE/ΣHREE, Sr/Br, Ce/La, Rb/Zr, CaO/(MgO×Al_2O_3), and V/(V + Ni) were also obtained from core samples in wells G3, H4, DJ43, DJ53, and Y787 . Values of V/(V + Ni) > 0.54, Sr/Br > 0.5, and Ce/La > 1.5 are interpreted as characteristic of a shallow-marine environment, the other values indicating a continental setting (*Rimmer, 2004*). Referring to the above critical condition, we obtained the relative regional sea-level fluctuation in accordance with the trace element in.

Transgression/regression rate calculation: based on the transgression/regression directions established above, we used 2D seismic data to identify the successive transgression events and calculate their distance of propagation (S). As indicated by the sediment thermal evolution history diagram previously obtained on these series (see *Yu et al., 2012*; *Ren et al., 2007*), the subsidence rates varied through time but remained spatially coherent (no large variations

243 throughout the study area at a given time). Subsidence was nearly null during the Pennsylvanian
244 interval, while it reached 30 m/Ma during the early Permian. Accordingly, the subsidence rate was
245 used as an input parameter in the transgression/regression rate calculationA following the
246 equation:

247 $$S= (D_{compaction} + D_{subsidence})/ \cos(\alpha),$$

248 $D_{compaction}$ is the decompacted thickness of mudstone in the strata; $D_{subsidence}$ is the
249 accommodation of regional subsidence; α represents the slope angle calculated from the
250 interpretation of the seismic profile.

251 Finally, by eliminating the subsidence impact factors, we calculated the
252 transgression/regression distance (S) using (v_{sea}) as $v_{sea} = S/T$, in which T is time.

253 ## 4. Lithofacies identification and association classification

254 During the transgression/regression process in the Carboniferous–Permian, the grain size and
255 lithology exhibited a dramatic change from conglomerate to mudstone. The series are also
256 containing well-identified layers of coal, limestone, quartz sandstone, and feldspar sandstone. In
257 this study, we defined 6 lithofacies associations using lithofacies previously established by *Zhu et*
258 *al. (2008*), *Yang et al. (2017)*, *and Xin et al. (2018)* in Ordos basin: massive mudstone (***M***);
259 bioturbated sandstone (***Sb***); muddy strip composite sandstone (***Scm***); slumped sandstone (***Sd***);
260 cross-bedding composite sandstone (***Scc***); cross-bedding sandstone (***Sc***); massive sandstone
261 (***Sm***); planar cross-bedded sandstone (***Sp***); massive gravel (***Gm***); planar cross-bedded gravel
262 (***Gp)*** (***FIG. 3*** and ***TABLE.1***).

263 ## 5. Identification of depositional environments from seismic and well data.

264 We selected two seismic profiles in an EW direction and calibrated them using wells G6 and

265 DJ12 as references. Based on this calibration, we defined depositional environments and created
266 a stratigraphic column.

267 **5.1 Pennsylvanian depositional environments**

268 As shown from core samples in well G6, the lithofacies association evolved upward from
269 LFA.5 to LFA.4, LFA.4, LFA.5, and finally LFA.6. Based on lithofacies interpretation in ***FIG.3***, the
270 early Pennsylvanian period was characterized by an initial bidirectional slow-rate traction flow
271 deposit, evolving upward toward a coarse-grained flow . Finally, facies LFA.5 and LFA.6 indicate
272 a weak hydrodynamic intensity during the late Pennsylvanian period. The cumulative grain-size
273 curve in ***FIG. 4*** also shows this last depositional environment evolution from a mass flow (g and f)
274 up to a tidal-dominated shallow-water setting (a to e). Additionally, *fusulinid* fossil typical of
275 shallow marine environments were observed at a depth of 2,431 m in well G6,(*Liu et al., 2015*).
276 The morphology of the GR curve also indicated the depositional environments in upward layers
277 as having been transient. In the early Pennsylvanian interval, the well-logging GR curve of
278 sandstone mainly showed a bell (2455m in G6 ***FIG.4***) or cylinder shape (2450 m in G6 ***FIG.6***),
279 indicating a rising sea level and an increase in flow dynamics. For the late Pennsylvanian interval,
280 the combination of the GR curve and the corresponding density curve (or sonic/neutron porosity
281 curve) highlight the occurrence of coal layers interbedded in limestone, characterizing a
282 decreasing sea level and a weakening flow rate. The Pennsylvanian period is thus marked by a
283 transgression phase followed by regression. However, regionally, the sea level showed a marked
284 spatiotemporal variability discussed below.

285 Well G6 was used to calibrate the facies pattern on the seismic line shown on ***FIG. 4.*** The
286 reflectors showing concave interfaces indicated erosion in tidal channel belts, while convex

interfaces are interpreted as sediment accumulation in tidal barriers. The tidal-dominated deposit (including the barrier and the tidal channel deposit) thus mainly developed during the early Pennsylvanian period.

5.2 Development of depositional environments during the early Permian period

The core samples in well DJ12 show a vertical evolution of lithofacies associations from LFA.6–LFA.2–LFA.1 (***Table 1***). The high-rate flow deposits of LFA.2 developed during the Asselian to Sakmarian interval. Deposition of LFA.1 including large mud clasts and lamellar cross-bedding indicate a slowing flow rate upward. As the cumulative grain-size curve in ***FIG. 5*** shows, two curve-pattern segments indicate a decreasing amount of suspended sediments and a flow-pattern evolution toward a one-directional traction flow. On the corresponding well-logs, the GR curve developed as a cylinder at the bottom and as a bell shape upward. This again indicate that the Asselian to Sakmarian interval can be divided into two cycles corresponding to a gentle transgression process.

FIG 5 displays a series of concave and convex seismic facies according to the seismic boundaries. Referring to the study of *Zhu et al. (2008)* and *Xin et al. (2018)*, we infer that braided channels (delta) initially developed, before being replaced upward by meandering channels. The seismic packages ascribed to the Asselian period show low amplitude and high continuity patterns. According to *Xin et al. (2018)*, the lateral migration events indicate that sandy sedimentary facies (such as braided delta) developed in the Asselian period, while upward toward the Sakmarian interval, we suggest that high amplitude and low continuity events represent a muddy depositional environment.

6. Results

6.1 Detrital zircon U–Pb data

Detrital zircons U-Pb age data are used to constrain the potential source area of sediments deposited in the Ordos basin during the Pennsylvanian to the early Permian. Four samples were selected in the early Permian series from various wells: DJ53 (1942.23 m Asselian), H5 (1968.1 m Asselian), DJ51 (2264.85 m Sakmarian), and G2 (2048.1 m Sakmarian) and representative zircon CL images are shown on ***FIG.6***. For the Pennsylvanian interval we refer to data from *Sun et al. (2014*) (samples JC-A and JC-B). Representative zircon CL images are shown in FIG. 6, Concordia plots in FIG.7 and individual age spectrums in FIG.8.

Samples JC-A and JC-B from the Bashkirian–Gzhelian stage are taken from *Sun et al. (2014*). Among the 94 detrital zircons in JC-A and 95 detrital zircons in JC-B, 83 (JC-A) and 94 (JC-B) have been considered adequate for dating (***FIG. 7***). Cathodoluminescence (CL) images show oscillatory zoning and Th/U ratios are generally over 0.1, indicating intermediate source rock types such as granitoids and metamorphic rocks (***FIG.9 a***). The obtained detrital zircon U-Pb ages can be divided into three groups: 273–307 Ma, 762–974 Ma, and 1168–2543 Ma.

In Asselian samples DJ53 and H5, zircon crystals are colorless, mostly elliptical (Fig. 6) and can be divided into three types according to their external morphology and internal structure. The first type is rounded/sub-rounded with a length/width ratio of 1:1.5 and shows a well-preserved magmatic oscillatory zoning. The second type has a length/width ratio of 1:3 and is angular/sub-angular shaped. The internal structure of zircons from this second group is either homogeneous or has patchy zoning. This kind of zircon constitutes 20% of each sample, and their age ranges from 1800 Ma to 1900 Ma (see crystals date at 1827 ± 20 Ma (DJ53) or 1803 ± 22 Ma (H5) on ***FIG. 6***). The third type of zircon is sub-rounded in shape and has a dark magmatic oscillatory

zoning implying a metamorphic source, especially for samples over 2000 Ma. A total of 180 crystals were analyzed for those two samples, and 168 of these, with a >90% concordance were considered adequate (age data in ***Appendix Tables 1 and 2***). The individual age are grouped into four classes: 310–375 Ma, 410–490 Ma, 1650–2300 Ma, and 2300–2500 Ma (***FIG. 7***).

Samples DJ51 and G2 were collected from the Sakmarian series. As shown in the CL image of ***FIG. 6***, zircon crystals of DJ51 and G2 are mostly angular/subangular with a length/width ratio of less than 2:1 and show a dark oscillatory zoning and bright overgrown homogeneous rim. The Th/U ratio ranging from 0.03 to 0.7 indicates intermediate rock sources. The U–Pb Concordia plots in ***FIG. 5*** shows that the concordance of all the grains (85 gains in DJ51 and 94 grains in G2) is over 90%. The U–Pb age spectrum of DJ51 and G2 reveals two groups at 275 to 450 Ma (peak value of 375 Ma) and 1750–2000 Ma.

6.2 Heavy mineral assemblages

Six types of heavy minerals (rutile, zircon, tourmaline, titanite, apatite and pyrite) were quantified from core samples and classified in five types using the Heavy Minerals Associations (HMA) of *Morton and Hallsworth (1994*) and the statistical approach of *Andrew (1985*) : rutile–dominated (HMA-I), pyrite–dominated (HMA-II), titanite–dominated(HMA-III), tourmaline–dominated, (HMA-IV), and zircon–dominated (HMA-V) (***FIG. 10***). In order to allow comparison, the HMA of potential source areas around the Ordos Basin, which includes the Qaidam–Qilian orogenic belt (QQOB) in the west, Yishan Orogenic belt (YOB) in the north, and Qinling orogenic belt(QOB) in the south, and their dominated HMA types are obtained from bibliography are listed in ***TABLE.2***.

The early Pennsylvanian deposits are characterized by HMA-II and HMA-III associations.

353 Similar associations, dominated by HMA-II are observed in the early Pennsylvanian deposits of
354 the QQOB, YOB suggesting common sediment sources(*Chen et al., 2009; Du et al., 2017*). The
355 pyrite content in wells Y521, H4, Y787, and Y653 is over 60%, which suggest that some sediment
356 may be transported from the QQOB. Besides that, we compared the HMA in DJ43, DJ53, and
357 that in the YOB (*Ruppen et al., 2014; Li et al., 2014*); both show HMA-III. Based on the increase
358 in that new source area we speculate that some sediment migrated far south from the northern
359 Ordos margin.

360 After the deposition of the late Pennsylvanian series, the pyrite content in well Y787 decreased
361 sharply, whereas the proportion of tourmaline considerably increased. This result suggests that
362 more sediment from the QQOB were either routed towards another basin or deposited in a
363 proximal area and not transported into the Ordos sink area. The well in the northern EMA
364 underwent an increase in zircon and rutile content, suggesting that a substantial amount of
365 sediment came from the YOB.

366 During the Asselian interval, the most represented heavy minerals are rutile, zircon, tourmaline,
367 titanite, apatite, and pyrite. The above can be further classified into three types of associations:
368 HMA-III , HMA-IV, and HMA-V. The average ZTR index in this interval shows an increase from
369 35% to 73%, indicating that the sediment was deposited in an increasingly distal area, and
370 detrital material from different provenance areas was mixed.

371 In the Sakmarian stage, the northern EMA showed an increase in titanite content in wells H4,
372 Y521, Y787, Y653, G3, and Y432, and the average grain size of heavy minerals increased from
373 0.01–0.15 mm to 0.02–0.03 mm. The average ZTR index shows a decreasing trend, from 52% to
374 31% that, together with the above parameters suggest a more proximal source, possibly in the

375 QOB affected by uplift at that period (Zhu et al., 2011; Dong et al., 2016).

376 **6.3 Trace element and REE patterns**

377 (1) Trace element and REE patterns

378 The chemical stability of La, Ce, Nd, Y, Th, Zr, Hf, Nb, Ti, and Sc during sediment migration
379 and the preservation in marine depositional environments of their concentration distribution
380 acquired in continental systems allow tracking source areas. In this study, we used the Hf–La/Th,
381 La–Sc–Co/Th, and ΣREE–La/Yb indexes to identify the mineral composition of the source rock
382 and their corresponding tectonic setting (***FIG. 11***). As shown by the Hf content ranging from 5.05
383 $\times10^{-6}$ to 8.33×10^{-6} and the La/Th ratio from 3.2 to 5.0., the lithology of the source rocks of the
384 Bashkirian to Sakmarian deposits is mainly felsic (***FIG. 11a***). This is further attested by the Co/Th
385 and La/Sc ratio of 0.47–1.93 and 2.73 – 8.40 respectively (***FIG. 11b***). The ΣREE ranges from
386 187.17 $\times10^{-6}$ to 751.75 $\times10^{-6}$ and the La/Yb ratio from 1.06 to 2.80 (***FIG 11c***). Finally, the La–Th–
387 Sc, Th–Co–Zr/10 and Th–Sc–Zr/10 plots in FIGS. 11d–e suggest that the tectonic setting of the
388 source area was intermediate between an active continental margin and island arc environment.

389 (2) Vertical evolution of the REE and trace element patterns in relation with sea-level
390 fluctuation

391 The ΣREE content of all analyzed samples ranges in (187.17–751.75) $\times10^{-6,}$ and its average
392 value is 299.83×10^{-6}, which is slightly higher than that in North American Shale Composite
393 (NASC (173.1×10^{-6})). ΣLREE ranges from 174.34×10^{-6} to 669.06×10^{-6}, and ΣHREE from
394 ($12.84\times10^{-6}$to $82.69\text{x}10^{-6}$. ΣLREE/ΣHREE is 8.09–16.44, and the average value is 11.44, which
395 is higher than that of NASC (7.50). The value of $(La/Sm)_N$ has a positive correlation with the
396 fractionating degree of the LREE, whereas $(Gd/Yb)_N$ can reflect that of HREE. As *McLennan et al.*

(1990) pointed out, an enrichment in LREE indicates a subaqueous setting; otherwise, HREE showed an aquatic setting. From the Bashkirian to the Gzhelian, we interpret the increase in ΣLREE/ΣHREE as indicative of a transgression phase. Similarly, the decrease in ΣLREE/ΣHREE during the Asselian to the Sakmarian is interpreted as marine regression.

As mentioned above, the trace elements ratio can also serve as an index of sea level variations (*Qiu et al., 2015*). During the early Pennsylvanian, the *w*(Sr)/*w*(Ba) of samples G3, DJ43, and DJ53 is over 0.5, and the *w*(Ge)/*w*(La) and *w*(Rb)/*w*(Zr) are over 1.5 and 0.75, respectively, which indicated a marine setting in the responding area. The *w*(Ge)/*w*(La) and *w*(Rb)/*w*(Zr) of samples H4 and Y787 in the western EMA is less than 1.5 and 0.75, which represent a continental setting. Thus, we speculate that the main transgression prograded westward.

During the Asselian stage, the (Sr)/*w*(Ba), *w*(Ce)/*w*(La), and *w*(Rb)/*w*(Zr) of Y787 showed a declining trend, whereas the *w*(V) / (*w*(Ni) + *w*(V)) and w(CaO)/w($MgO \times Al_2O_3$) indices increased to over 0.25 and 0.75. These results indicate that the sea level rose sharply during the Asselian stage; this conclusion is the similar to that of *Xin et al. (2018*). During the Sakmarian, w(Sr)/w(Ba) in G3 decreased sharply to 0.2, indicating a regression process in the southern EMA. Combining the trace element ratio and the study of *Zhu et al. (2008*), we infer that the main regression was ESE directed.

6.4 $\delta^{18}O$ and $\delta^{13}C$ data

The $\delta^{18}O$ and $\delta^{13}C$ data obtained on whole-rock samples show the fluctuation trend of the sea level caused by climate or the sediment rate change (***FIG. 14***). During the Pennsylvanian, $\delta^{13}C_{V\text{-}PDB}$ ranged from −8‰ to −25‰, and $\delta^{18}O_{V\text{-}PDB}$ ranged from −5‰ to −15‰. The value shows a

419 negative excursion and a decreasing trend, indicating an warming climate and more rainfall. This
420 result is consistent with the study of *Montanez et al. (2007*) *and Haq and Schutter (2008)*. During
421 the Asselian–Sakmarian, $\delta^{13}C_{V\text{-}PDB}$‰(−4.35‰–−1.36‰) and $\delta^{18}O_{V\text{-}PDB}$‰(−9.42–−11.35) showed
422 a positive excursion, which speculate the sea level rising during this interval.

423 **6.5 Paleontological assemblage**

424 During the Pennsylvanian, the value of w_{leaf} (the amount of preserved leaf in macro-plant
425 remnants) showed a rising trend from 0.47 to 0.52 including species such as *Cathaysiodendron*
426 *nanpiaoense*, *Conchophyllum richthofenii*, *Alloiopteris sp.,* and *Lepidodendron cf. szeianumis*. In the
427 early Pennsylvanian series, leaf remnants are generally fragmented and mixed with stems
428 fragments (***FIG. 15,*** samples G10 and DJ28). In the late Pennsylvanian, the w_{leaf} increased to
429 0.52, suggesting a rising sea level; whereas the large proportion of complete leaf remnants (***FIG.***
430 ***15*** G7 and H5) suggests a weakening hydrodynamic setting.

431 During the early Permian, the amount of plant fossils sharply increased, and the $w_{biomass}$ of
432 ferns such as *Lycopsids*, *Emplectopteris,* and *Emplectopteridium,* showed a sudden decrease during
433 the transition from Kasimovian to Asselian. The root and stem fossils were predominant during
434 the Asselian interval (***FIG. 15*** G1), and the ratio of the broad leaf remnants(w_{leaf}) decreased to
435 0.30. Up to the Sakmarian interval, the stem fragments keep predominant, whereas the w_{leaf}
436 declined to 22%.

437 **6.6 Clay minerals distribution**

438 As indicated above, continental sediment generally show a high chlorite and/or kaolinite
439 content while marine sediment may show a high illite content. Furthermore, *Raucsik and Varga,*
440 *(2008)* and *Chamley et al., (1993)* showed that differential settling of clay minerals during

441 sedimentation processes could explain the illite and smectite enrichment in marine settings away
442 from the major river deltas and estuaries Triangle diagrams showing the proportion of each type
443 of clay (chlorite and kaolinite are plotted on the same location) are thus use to infer the
444 continental, shallow-marine or deep-marine depositional environment through time (FIG.16).

445 Northeastern part of the EMA: Wells DJ16 and DJ43 (***FIG. 16)*** are characterized by a high
446 chlorite content (>50%) in the Pennsylvanian, which shows an increasing in illite content
447 characterizing the late Pennsylvanian (Kasimovian), which rise from 20% to 45%. whereas,
448 chlorite and kaolinite are still predominant *(w_{clay}* (the ratio of *w*(chlorite + kaolinite)/*w*((illite))values
449 are still over 1.0), indicate that the sediments from a continental setting is dominated in this
450 interval. During the Asselian stage, the illite content of wells DJ16 and DJ43 decreased to 35%,
451 further supporting the occurrence of a slight regression phase and an increasing input of
452 continent-derived detrital material.

453 Southeastern part of the EMA: In wells DJ53 and DJ30 illite dominated (their content high up
454 to 50%) during the Pennsylvanian to Sakmarian. All the above data indicate that the sediment
455 deposited in the southern EMA may be below the sea level.

456 Southwestern part of the EMA: The Pennsylvanian section in well G3 shows a high chlorite
457 content (>50%), and a w_{clay} index over 1.5, indicating that the southwestern part of the EMA is
458 below the sea level up to the late Pennsylvanian. With the illite content decreasing dramatically
459 (from 35% to 25%), we infer that a regression progress occurred in the southwestern block during
460 the early Permian.

461 Northwestern part of the EMA: In well H4, chlorite and kaolinite dominate the clay spectrum
462 from the Pennsylvanian to the Sakmarian, indicating a terrestrial depositional setting. As to the

463 Asselian–Sakmarian, the chlorite content in Y787 shows a decreasing trend (from 65% to 50%),
464 indicating less sediment input from continental source regions.

465 7. Provenance area identification and sediment supply calculation

466 7.1 Provenance

467 7.1.1 Provenance area during the Pennsylvanian

468 Based on published U-Pb data from *Yang et al. (2005*), *Darby and Gehrels (2006), Li et al.*
469 *(2013), and Sun et al. (2014)* we obtained the main characteristics of potential provenance areas
470 in the Qinling orogenic belt (south), the Qaidam–Qilian orogenic belt (west) and the Yinshan
471 orogenic belt (north)(***FIG. 8***). Furthermore, *Xie and Heller (2013*) pointed out that late Paleozoic
472 uplift in the north China block may also be a potential source area for the Ordos basin. The age
473 spectrum of JC-A and JC-B (early Pennsylvanian) show a major zircon U-Pb age population at
474 762–974 Ma, similar to the one observedin the Qaidam–Qilian orogenic belt (***FIG. 8***). As for the
475 peak point at 1750 Ma, we speculate that some sediment came from the Yinshan orogenic belt.
476 According to ***FIG. 11 d*** and ***f***, the trace elements pattern of the early Pennsylvanian samples
477 suggest a source mainly composed of continental island arc and active continental margin
478 lithologies, again suggesting a source in the Qaidam–Qilian and Yinshan orogenic belts (*Darby*
479 *and Gehrels,2006*); *Golonka and Ford, 2000)*. Finally, both HMA (samples DJ43 and DJ53) and
480 ZTR indexes indicate a distal deposition process compatible with a source in the Qilian Shan and
481 Yinshan (***FIG. 10***).

482 7.1.2 Provenance area during the early Permian

483 The zircon U-Pb age population of 310–375 Ma recorded in the age spectrum of samples H5,
484 DJ53, DJ51, and G2,is largely comparable to the one shown in samples from the Qinling orogenic

belts (*Sun et al., 2014; Xin et al., 2018*). Furthermore, *Zhu et al., 2011 and Dong et al., 2016,* indicated a source from the Qinling orogenic belt in the early Permian southern EMA deposits. Trace elements and REE patterns further indicate that the material was largely derived from Paleozoic sedimentary rock or igneous rock (as Sample E shown in ***FIG. 12***) (*Shi et al., 2018*). Thus, we speculate that some of the early Permian sediment originated from the Qinling region. The Asselian record of wells H5 and DJ53 show two other zircon U-Pb age peaks at 1650–2300 and 2300–2500 Ma. Based on the analogy with the age spectrum obtained by *Darby and Gehrels(2006*)we infer that some of the material also derived from the Yinshan orogenic belt. The increase observed in the ZTR index support that hypothesis of a more distal source.

In the Sakmarian stage, these two zircon U-Pb age peaks are absent from the age spectrum (***FIG. 8),*** especially for the wells in the southern EMA (G2). Based on the HMA index (***FIG. 10***), we speculate that the provenance area of the sediment in the northern EDM is mainly the northern Ordos margin through long-distance transport. As to the southern EMA, the decreasing ZTR index indicates a switch from distal provenance to a more proximal source. Moreover, the detrital zircon U-Pb age spectrum and trace elements distribution (FIG 8 and 11) reflects material issued from the Yinshan and Qinling orogenic belt.

7.2 Sediment supply rate calculation

We selected two profiles to calculate the sediment deposition rate in the EMA. ***FIGS. 17 and 18*** show the EMA in the N–S and E–S direction, respectively. We divided the profile into four layers: Penzi Formation (Ct–Cb), Taiyuan Formation (Cb–P2s), Upper Shanxi Formation (P2s–Pt10), and Lower Shanxi Formation (Pt10–Ps1).

7.2.1 Pennsylvanian sedimentation rates

As shown in the well calibration (***FIG. 1)***, the Moscovian–Kasimovian stage in the early Pennsylvanian is represented by the Penzi Formation, while the Taiyuan Formation formed during the Gzhelian stage.

Then, we evaluated the strata thickness (A) on the basis of the seismic profile in ***FIGS. 17*** and ***18***. During the Moscovian–Kasimovian stage (315.2~303Ma), the sediment from the eastern EMA was deposited , and its transport path showed a east direction as that in ***FIG. 18***. The statistical mean thickness of the strata (A) in a series of the E–W direction profiles range from 70 m to 90 m. Thus, the average sedimentation rate at this stage is 8 m/Ma, whereas the minimum sedimentation rate is 5 m/Ma. During the Gzhelian stage, the decrease in the strata thickness to 10–20 m corresponds to a declining trend of the sedimentation rate (2~4m/Ma) interval. The low sedimentation rate in the Gzhelian (*Jiang and Wang, 2012; Xu et al., 2015*) is directly related to the formation of the carbonate platform in the EMA, as the clastic input largely decreased.

7.2.2 Early Permian sedimentation rates

The Asselian stage is represented by the Lower Shanxi Formation, and the Sakmarian by the Upper Shanxi Formation .

We selected a seismic profile in the 2D block, consistent with the sediment migration direction. According to the above study, sediment was mainly transported from the northern EMA during the Asselian stage (***FIG. 17)***. During the Sakmarian, sediment was transported from two directions: the southern EMA was filled by proximal material from QOB(Qiling Orogenic belt), whereas the northern block was filled sediment from a distal area(YOB: Yinshan Orogenic belt). Thus, as the static data in ***Table 3***, we evaluate the sedimentation rate in the southern EMA and calculated the sedimentation rate in the northern block on the basis of ***Table.3***.

As shown in ***FIG. 18***, the average strata thickness (A) of the Lower Shanxi Formation (Asselian298~295Ma) is 80–100 m, and the calculated sedimentation rate is 20–25 m/Ma. In the Upper Shanxi Formation (Sakmarian), more sediment were provided and the sedimentation rate reached 30 m/Ma in the southern block and 20~25 m/Ma in the north E.M.D. .

7.3. Transgression/regression rate calculation

7.3.1 Transgression/regression rate during the Pennsylvanian

As shown in ***FIGS.16a*** and ***16b***, the main transgression/regression direction during the Pennsylvanian is E–W in the northern block, whereas that in the southern block is N–NW. According to the profiles with a similar direction of transgression/regression as that of the northern block, the seismic packages (TP9–TP10) in ***FIG. 18*** are characterized by high continuity and low onlap . These characteristics indicate limited erosion during the sea level rising process. *Jiang and Wang. (2012*) *and Xu et al. (2015)* suggested that the transgression process in the Pennsylvanian was mainly controlled by accommodation changes. The average transgression rate during the Pennsylvanian was 15 km/Ma (T.P.1~4 and 8~10 ***TABLE 3***). As to the southern block, the seismic packages showed an onlap from TP1 to TP3, indicating that the regional subsidence provided enough accommodation space for the sediment. Considering the distance from TP1 to TP3, the transgression rate on the southern block during the Pennsylvanian period was 7.6 km/Ma. Trace elements, $\delta^{18}O$ and $\delta^{13}C$, and paleontological assemblages show a sharp regression event during the late Pennsylvanian (Kasimovian) (***FIGS. 13, 14, and 15***). However, the resolution of the seismic profile makes it impossible to calculate the regression rate during that period.

7.3.2 Transgression rate from the Asselian to the Sakmarian stage

FIGURE 16c shows an NW–W directed transgression during the Asselian stage. We selected ***FIG. 18*** to calculate the transgression rate. The TP13 and TP14 markers were chartered by a series of discontinuous seismic packages and distinct concave reflection boundaries. We calculated the average transgression of the EMA as 30 km/Ma. During the Sakmarian stage (***FIG. 16d***), sea level variations occurred in a spatially variable pattern caused by the uplifting process in the southern orogenic belt. More proximal sedimentation lead to a sharp regression in the southern EMA. According to the seismic packages RP4, RP5, and RP6 (***FIG .17***), we obtained a regression rate of 50 km/Ma. In the northern block, the calculated average regression rate ranges from 15 km/Ma to 20 km/Ma according to the seismic packages RP9 and RP10 (***TABLE 3***).

8. Mechanism of transgression or regression in intracratonic basin

After calculating the sedimentation rates and the transgression/regression rates, we reconstructed the S2S system during the Carboniferous–Permian (***FIG. 19***) in accordance with the BQART model of *Syvitski and Milliman (2007*). (***FIG. 20***) and classified it into three types: low-transgression rate and less-sediment supply S2S pattern (LT–LS) during the Pennsylvanian period, high-transgression rate and massive sediment supply S2S pattern (HT–MS), and low-transgression rate and massive sediment supply S2S pattern (LT–MS) during the Asselian to Sakmarian stage. Below, we infer the mechanism of Carboniferous–Permian transgression in accordance with the quantitative parameters of the S2S system.

8.1 S2S distribution pattern between the interglacial and glacial epochs

During the early Pennsylvanian (Bashkirian–Kasimovian), the EMA mainly developed tidal deposits. We distinguished the N-S directed tidal barriers, which developed on the former basement (*Shen et al.,2017*), separating the EMA from the western part of the Ordos Basin (both

sub-basins were evolving independently). In addition, the provenance study shows that the sediment came from a distal area in the western margin (***FIG. 19c)***. Combining the above depositional setting, meandering channels in the western block and tidal channels in the eastern EMA (***FIG. 19a)***. With the decrease in sedimentation rate and the increasing transgression area, the carbonate platform developed during the late Pennsylvanian period (Gzhelian) along the western EMA; the lithofacies also support this conclusion. Thus, we infer that the shallow-marine areas in the early stage. At the same period, the western sub-basin is characterized by floodplain and channel deposits (*Zhang et al. 1997*) associated a low-transgression rate and less-sediment supply (LT–LS S2S pattern) (***FIG. 20***a). Then, refer to the study of (*Michael et al., 2013;Hampson et al., 2014*), this pattern of S2S system further shows mass sediment attested by fine-grained deposits infills.

During the Asselian stage, the depositional setting constrained from seismic data shows a series of erosion channels (***FIG. 4 and 5***). At the same time regression continues in the western Ordos Basin, leading to shelf and floodplain depositional environments. *Ritts et al., (2006*), and *Zhang et al., (1997)* pointed out that the facies association include braided- and meandering/anastomosed- channels (***FIG. 19***). The sedimentation and transgression/regression rates calculated above reveal that the high-transgression rate and mass sediment supply (HT–MS) (***FIG. 20***b) pattern was predominant during this interval. During the Sakmarian stage, the sediment input from the Yinshan orogenic belt declined slightly providing less coarse-grained material. We distinguished facies associations LFA.1 and LFA.3 during this interval and interpret it as a meandering channel. The S2S system that developed in the northern EMA had an HT–MS pattern. By contrast, the southern block developed various S2S systems. From the facies

association (FIG. 4), we conclude that delta fan or coarse-grained delta depositional environments dominated during this interval. Thus, we infer that the Asselian–Sakmarian stage with massive sediment input corresponds to the interglacial period. The S2S system in the southern block shows a typical low-transgression rate and massive sediment supply (LT–MS) S2S pattern (***FIG. 21***c). In the southern block, coarse-grained submarine fans or delta fans developed in proximal areas. In the northern EMA, sedimentation occurred with more distal than the southern one..

8.2 Mechanism of transgression from the perspective of the S2S system

Based on the depositional environments (***FIG. 19***) and reconstruction of the topography of the basin derived from seismic data (***FIG. 17 and 18***), we propose the following S2S pattern model.

1) LT–LS S2S pattern (Pennsylvanian)

The topographic reconstruction of the Pennsylvanian basin indicates low continental slopes. The stratigraphy indicates a limited carbonate platform and shallow waters characterized by tidal-influenced deposits. Then, we calculated the parameters (***TABLE 3***) of the LT–LS S2S pattern during the Pennsylvanian and built the response equations as follows:

$$V = aA + bS + c\alpha \cdot e^{H} + m, \qquad (\textbf{\textit{FIG. 20d}})$$

where V is the volume of the S2S system, which can be obtained from the seismic data; A is the distance between the provenance area and the sink area; S represents the sedimentation rate; *α shows the dip angle of the slope; and H is the relative sea level.* a, b, and c in the equation are obtained in accordance with the fitting of the data in ***TABLE 3***.

As stated above, the volume of the S2S system during the Pennsylvanian is limited, and most sediment accumulated on the slope (***FIG. 20a)***. The bubble chart shows that α is inversely

proportional to the relative sea level (H). We infer that the key factor controlling the relative sea (H) level is the variations in slope dip (α). *Lan et al. (2016*) also pointed out that the spatial variability transgression direction is caused by topographic variations. On this basis, as the general slope (shown as the morphology map in ***FIG.16***), we can explain the fast transgression in the northern EMA and the slow transgression rate in the southern block.

2) HT/LT–MS S2S pattern

The facies association pattern in FIG. 19 shows a spatially varible evolution in the south and north block of the EMA during the Asselian–Sakmarian. As to the northern part, the stratigraphy indicates braided channels or meandering/anastomosed rivers. The southern part was dominated by fan deltas or alluvial fans. Then, we statistically calculated the S2S parameters in the Asselian–Sakmarian (***TABLE 3***) and obtained the following fitting equation:

$$V = a\alpha \cdot A \cdot H + be^{S} + m. \qquad (\textbf{\textit{Fig. 20e}})$$

In the HT–MS system, the volume of the S2S system is affected by the sedimentary supply (S) and the relative sea level (H). For the Sakmarian interval, we assumed that V is a determined value. The relative sea level (H) is inversely proportional to the sedimentary supply (S). Furthermore, Zhu et al., (2008) pointed the subsidence rate keep stable during this interval. Thus, we speculate that in the HT–MS system the sedimentation rate is the key factor driving the sea level.

As to the LT–MS system in the southern block, we statistically calculated the S2S parameters during the Sakmarian and obtained

$$V = a\alpha \cdot A \cdot H \,.S + m. \qquad (\textbf{\textit{Fig. 20f}})$$

The bubble chart in ***FIG. 20 f*** shows that the accumulated sediment and the dip angle can

affect sea-level fluctuation as generally inferred in sequence stratigraphy studies (*Zhu et al., 2008*). Due to the uplift caused by the formation of the Qinling orogenic belt, the slow transgression rate, and the fast regression rate during the Sakmarian were mainly controlled by the substantial amount of sediment accumulated and the increase in dip angle.

9. Conclusion

1. During the Pennsylvanian, sediments mostly came from the Qaidam–Qilian orogenic belt and were deposited in a distal setting. Some distal sediments from the northern margin of the Ordos Basin were injected in the dispersal area. The sediment accumulation rate during this interval ranges from 5 m/Ma to 10 m/Ma. During the Asselian–Sakmarian interval, material was derived from multiple provenance areas. The sediment from the Qinling orogenic belt accumulated at a rate of 30 m/Ma, and that from the western and northern Ordos Basin accumulated at 10 and 30 m/Ma, respectively. The timing of sedimentation rate changes is synchronous with the interglacial–glacial process in the early Permian.

2. During the early Pennsylvanian, transgression occurred towards the NEE, and the relative horizonal transgression rate reached as high as 15 km/Ma. We classified this kind of S2S pattern as LT–LS. During the Asselian stage, transgression occurred toward the NNW with a rate of 30 km/Ma. During the Sakmarian, the sea level rose again, and the direction of transgression in the EMA was NW. The transgression rate was up to 50 km/Ma. We also identified two different S2S patterns, that is, LT–MS in the south and HT–MS in the north.

3. In the LT–LS pattern, the transgression/regression process was dominated by the dip angle of the morphology due to lower sediment supply during the glacial period (Pennsylvanian). In this pattern, the intensive reworking flow determined the region where coarse-grained sediments

developed. As the S2S pattern transitions to the HT–MS or the LT–MS pattern, we speculate that the migration of the sediment distance is a key factor that influences the transgression/regression process.

Acknowledgments

This research was sponsored by the Major State Science and Technology Research Program and China Scholarship Council (CSC) (No. 201906400071). The authors wish to thank the coalbed methane company, China National Petroleum Company, for providing the geological and seismic data used in this work. We also wish to acknowledge the Paleo-2D team of Université de Rennes 1, France, and the sedimentology team of the China University of Geoscience, Beijing. The authors also thank the journal reviewer and handling editor for their thoughtful and useful comments, which helped to improve the quality of this manuscript.

Figure Captions

FIG. 1

Geomorphological map of the North China Block. a. Faults developed in the Ordos Basin. The area with the dotted line is the EMA in the Ordos Basin. The generalized stratigraphic column is shown in the left. Seismic data calibration and the stratigraphic maker referred to the study of *Zhu et al. (2008*). From bottom to top: Penci Formation, Taiyuan Formation, Shanxi Formation, and Shihhotse Formation.

FIG. 2

The stratigraphy developed in Y787, DJ53, DJ43, H4, and G3. From left to right of each well is the Grammy curve, lithology. With the zircon age data shown in DJ53 and the related reference

683 (***Sun et al., 2014; Sun et al., 2013; Wang et al., 2003***), we identified the deposited age of layers,
684 including the Penzi Fm. Taiyuan Fm, Lower Shanxi Fm. and Upper Shanxi Fm. Litho.=Lithology,
685 Chronolo.=Geochronology.

686 **FIG. 3**

687 Lithofacies templates. Seven kinds of lithofacies associations are provided on the right side.
688 From left to right: slow-rate one-directional traction flow deposited; high-rate one-directional
689 tractional flow, slow-rate bidirectional traction flow, mass flow deposited, static water deposited
690 and carbonated plate deposited.

691 **FIG. 4**

692 From left to right shows the seismic profile, well log of G6 and their responding cumulative
693 grain-size curve. We interpreted the lithofacies according to the core sample calibration. The
694 sandstone can be identified by the low GR value, while the limestone is characterized by the low
695 DEN value. Furthermore, integrated the well log and the seismic reflection, we interpreted the
696 facies association in the Pennsylvanian, including the tidal channel and the barriers.

697 **FIG. 5**

698 From left to right shows the seismic profile, well log of DJ12 and their responding cumulative
699 grain-size curve. The cross-bedding in LFA.1 and LFA.2 indicated a tractional flow developed.
700 Calibrated these on the seismic data, we recognized a series of the erosion channel developed.

701 **FIG. 6**

702 Representative zircon CL images. The small white circles represent the sites of U–Pb age
703 analyses, and the measured ages are shown in Ma.

704 **FIG. 7**

705 Concordia plot of the detrital zircon of JC-A and JC-B (a), H5 and DJ53 (b), G2 and DJ51 (c).
706 Data influenced by Pb loss and inclusion are deleted. Only analyses with concordances of >90%
707 are included in the combined probability density plot and histogram and discussed in the
708 subsequent sections.

709 **FIG. 8**

710 Zircon U–Pb age spectra of the Paleocene sediment in JC-A, JC-B, H5, DJ53, DJ51, and G2.
711 Potential source area: Qinling orogenic belt, Qaidam–Qilian orogenic belt, Yinshan orogenic belt,
712 West North China Block *(Xie and Heller, 2013; Kröner et al., 2006; Darby and Gehrels, 2006; Zhu*
713 *et al., 2011*).

714 **FIG. 9**

715 As *Hoskin and Black (2000)* and *Teipel et al. (2004)* pointed out the according to the ratio of
716 Th/U value, we can infer the sediment are mainly provided by the igneous sources (Th/U over
717 0.5), or the metamorphic sources (Th/U less than 0.1). And the Th/U value between the 0.2 and
718 0.5 indicate a mixture of the igneous and metamorphic source. Intersection diagrams for the Th/U
719 ratio and age distribution. From left to right: samples of the Bashirian–Gzhelian, Asselian, and
720 Samarian stages.

721 **FIG. 10**

722 HMA of Y521, H4, Y787, Y653, G3, Y432, DJ43, and DJ53. We classified the HMA into five
723 types: rutile–prominent (rutile>60%), pyrite–prominent (pyrite>60%), titanite–prominent
724 (titanite>50%), tourmaline–prominent (tourmaline>30%), and zircon–prominent (zircon>30%)
725 EMA=East Margin area of Ordos Basin

726 **FIG. 11**

Points in the source rock discrimination chart show the tectonic setting of the EMA sediment. The first line shows Hf–La/Th (a), La/Sc–Co/Th (b), and ΣREE–La/Yb (c). The second line from left to right shows the La–Th–Sc, Th–Co–Zr, and Th–Sc–Zr.

FIG. 12

(a) Geological map of the Ordos Basin. We selected samples A, B, C, D, E, F, and G (b) around the EMA to study their clay mineral distribution. (c) represents the REE distribution in the Pennsylvanian with data from DJ28, DJ43, and DJ53. ΣLREE/ΣHREE is 8.09–16.44/11.44; (d) and (c) are the REE distribution in the Asselian and Sakmarian, respectively. We obtained the value of ΣLREE/ΣHREE in the Asselian is 9.74–15.72/10.12, whereas its value in the Sakmarian is 8.01–11.62/9.12. These values indicate the regression process during the Asselian and Sakmarian.

FIG. 13

Trace element vertical distribution in G3, H4, DJ43, DJ53, and Y787.

FIG. 14

$\delta^{18}O$ and $\delta^{13}C$ data vertical distribution in Y787, DJ53, DJ 43, H4, and G3.

FIG. 15

Column from left to right show the w_{leaf} index, $w_{biomass}$ index, micropaleontological assemblage (*Pfefferkorn and Wang, 2007*), and the plant fossils in the core samples. Referring to the statistical data of paleontological assemblage, we found that the sea level of the EMA increased during the Pennsylvanian and declined sharply during the Asselian–Sakmarian.

FIG. 16

We built the paleomorphology on the basis of 2D seismic data and the relative sea level as the

749 w_{clay} index. From bottom to top: paleo-sea level developed from the early Pennsylvanian (a), the
750 late Pennsylvanian (b), the Asselian (c), and the Sakmarian (d).

751 **FIG. 17**

752 The seismic profile in the N–S direction and the location is shown in ***FIG. 1.*** We distinguished
753 a series of tidal channel with the swing channels as the concave of the seismic event. As to the
754 late Pennsylvanian (Gzhelian), the limestone developed and showed a continuous and high
755 amplitude reflection. Referring to *Zecchin et al. (2008*), we distinguished a series of forest seismic
756 packages and numbered them as TP1 to RP6.

757 **FIG. 18**

758 The seismic profile in the W–E direction and the location is shown in ***FIG. 1.*** We distinguished
759 a series of forest seismic packages and numbered them as TP8 to RP10.

760 **FIG. 19**

761 (a) to (c) show the patterns of the three stages of the S2S system evolution during the
762 Pennsylvanian and Asselian to Sakmarian. During the first stage, sediment migrated from a distal
763 area, and a barrier developed on the slope. With the provenance area transfer, the north Yinshan
764 orogenic provided mass sediment in this interval. During the third stage, the Qinling orogenic belt
765 formed and lead delta fan developed in the southern block. We classified the S2S system of the
766 first stage as a low-transgression-rate and less-sediment-supply S2S pattern. The second stage
767 and the sediment rounding system in the northern block during the third stage has a high-
768 transgression-rate and mass-sediment-supply S2S pattern, whereas the southern block in the
769 third stage has a low-transgression-rate and mass-sediment-supply S2S pattern.

770 **FIG. 20**

S2S parameters (a to c) marked in the sections, including the bed evaluation height, the sediment supply and the relative sea level. Then, we fit these parameters (in ***TABLE 3***) and obtained the balloon chart (d to f). The diameter represents the volume of the S2S system, and we can speculate the mechanism for the transgression/regression process in accordance with the fitting equation.

Table Caption

Table 1

Facies association descriptions.

Table 2

Heavy mineral assemblage in the potential source.

Table 3

Parameters of the S2S system. Statistical data were based on seismic data. We obtained the dip angle with the slope dip along the slope.

Reference

Adkins, J.F., McIntyre, K. and Schrag, D.P., 2002. The salinity, temperature, and delta18O of the glacial deep ocean. ***Science***, 298(5599): 1769-73.

Alkmim, F.F. and Martins-Neto, M.A., 2012. Proterozoic first-order sedimentary sequences of the São Francisco craton, eastern Brazil. ***Marine and Petroleum Geology***, 33(1): 127-139.

Andrew, M., 1985. A new approach to provenance studies: electron microprobe analysis of detrital garnets from Middle Jurassic sandstones of the northern North Sea. ***Sedimentology***, 32(4): 553-566.

Anees, A., Shi, W., Ashraf, U. and Xu, Q., 2019. Channel identification using 3D seismic

attributes and well logging in lower Shihezi Formation of Hangjinqi area, northern Ordos Basin, China. ***Journal of Applied Geophysics***, 163: 139-150.

Bacon, K.L., Haworth, M., Conroy, E. and McElwain, J.C., 2016. Can atmospheric composition influence plant fossil preservation potential via changes in leaf mass per area? A new hypothesis based on simulated palaeoatmosphere experiments. ***Palaeogeography, Palaeoclimatology, Palaeoecology***, 464: 51-64.

Blum, M.D. and Törnqvist, T.E., 2000. Fluvial responses to climate and sea-level change: a review and look forward. ***Sedimentology***, 47: 2-48.

Bumby, A.J., Eriksson, P.G., Catuneanu, O., Nelson, D.R. and Rigby, M.J., 2012. Meso-Archaean and Palaeo-Proterozoic sedimentary sequence stratigraphy of the Kaapvaal Craton. ***Marine and Petroleum Geology***, 33(1): 92-116.

Chamley, H., Angelier, J. and Teng, L.S., 1993. Tectonic and environmental control of the clay mineral sedimentation in the late Cenozoic orogen of Taiwan. ***Geodinamica Acta***, 6(2): 135-147.

Chen, Q., W. Li, H. Liu, K. Li, J. Pang, Y. Guo, and Z. Yuan, 2009, Provenance analysis of sandstone of the Upper Carboniferous to Middle Permian in Ordos basin. ***Journal of Palaeogeography, with English abstract***, 11(6): 629-640.

Cheng, C., S. Li, X. Xie, T. Cao, W. L. Manger, and A. B. Busbey, 2019. Permian carbon isotope and clay mineral records from the Xikou section, Zhen'an, Shaanxi Province, central China: Climatological implications for the easternmost Paleo-Tethys. ***Palaeogeography, Palaeoclimatology, Palaeoecology***, 514: 407-422.

Darby, B.J. and Gehrels, G., 2006. Detrital zircon reference for the North China block. ***Journal of Asian Earth Sciences***, 26(6): 637-648.

De Falco, G., F. Budillon, A. Conforti, M. Di Bitetto, G. Di Martino, S. Innangi, S. Simeone, and R. Tonielli, 2015. Sorted bedforms over transgressive deposits along the continental shelf of western Sardinia (Mediterranean Sea). ***Marine Geology***, 359: 75-88.

Dong, Y., Z. Yang, X. Liu, S. Sun, W. Li, B. Cheng, F. Zhang, X. Zhang, D. He, and G. Zhang, 2016, Mesozoic intracontinental orogeny in the Qinling Mountains, central China: ***Gondwana Research***, 30: 144-158.

Du, J., S. Zhang, W. Xiao, and W. Jiang, 2017, Geochemistry Characteristics of Middle-Lower Jurassic Clastic Rocks in the Northern Margin of Qaidan Basin and Their Geological Significance: ***Journal of Earth Sciences and Environment, with English abstract***, 39(06): 721-734.

Elderfield, H., P. Ferretti, M. Greaves, S. Crowhurst, I. N. McCave, D. Hodell, and A. M. Piotrowski, 2012. Evolution of Ocean Temperature and Ice Volume Through the Mid-Pleistocene Climate Transition. ***Science***, 337(6095): 704-709.

Fu, C., Huang, W., Li, S. and Chen, H., 2019a. The spatial discrepancy of Miocene transgression and its corresponding channel transformation pattern: A case study of the carabobo region in the northeast Venezuela basin. ***Journal of South American Earth Sciences***, 89: 347-365.

Fu, C., Li, S., Li, S., Fan, X. and Xu, J., 2019b. Sedimentary characteristics, dispersal patterns, and pathway formation in Liaoxi Sag, Liaodong Bay Depression, North China: Evolution of source-to-sink systems in strike-slip tectonics belt. ***Geological Journal***.

Gastaldo, R.A., 2004. The relationship between bedform and log orientation in a Paleogene fluvial channel, Weißelster Basin, Germany: implications for the use of coarse woody debris for paleocurrent analysis. ***Palaios***, 19(6): 587-597.

Gee, C.T., 2005. The genesis of mass carpological deposits (bedload carpodeposits) in the Tertiary of the Lower Rhine Basin, Germany. ***Palaios***, 20(5): 463-478.

Golonka, J. and Ford, D., 2000. Pangean (late Carboniferous–Middle Jurassic) paleoenvironment and lithofacies. ***Palaeogeography, Palaeoclimatology, Palaeoecology***, 161(1-2): 1-34.Haq, B.U. and Schutter, S.R., 2008. A chronology of Paleozoic sea-level changes. ***Science***, 322(5898): 64-68.

Haq, B.U., Hardenbol, J. and Vail, P.R., 1987. Chronology of fluctuating sea levels since the Triassic. ***Science***, 235(4793): 1156-1167.

Hilton, J. and Cleal, C.J., 2007. The relationship between Euramerican and Cathaysian tropical floras in the Late Palaeozoic: Palaeobiogeographical and palaeogeographical implications. ***Earth-Science Reviews***, 85(3-4): 85-116.

Hoffmann, K. L., J. M. Totterdell, O. Dixon, G. A. Simpson, A. T. Brakel, A. T. Wells, and J. L. Mckellar, 2009. Sequence stratigraphy of Jurassic strata in the lower Surat Basin succession, Queensland. ***Australian Journal of Earth Sciences***, 56(3): 461-476.

Hoskin, P. and Black, L.P., 2000. Metamorphic zircon formation by solid-state recrystallization of protolith igneous zircon. ***Journal of metamorphic Geology***, 18(4): 423-439.

Ichaso, A.A. and Dalrymple, R.W., 2009. Tide- and wave-generated fluid mud deposits in the Tilje Formation (Jurassic), offshore Norway. ***Geology***, 37(6): 539-542.

Jiang, Z., Xu, J. and Wang, G., 2012. The discovery and significance of a sedimentary hiatus within the Carboniferous Taiyuan Formation, northeastern Ordos Basin, China. ***AAPG Bulletin***, 96(7): 1173-1195.

Kemp, D.B. and Izumi, K., 2014. Multiproxy geochemical analysis of a Panthalassic margin record of the early Toarcian oceanic anoxic event (Toyora area, Japan). ***Palaeogeography, Palaeoclimatology, Palaeoecology***, 414: 332-341.

Klein, G.D., 1982. Probable sequential arrangement of depositional systems on cratons. ***Geology***, 10(1): 17.

Koch, J.T. and Frank, T.D., 2011. The Pennsylvanian–Permian transition in the low-latitude carbonate record and the onset of major Gondwanan glaciation. ***Palaeogeography, Palaeoclimatology, Palaeoecology***, 308(3-4): 362-372.

Kröner, A., S. A. Wilde, G. C. Zhao, P. J. O Brien, M. Sun, D. Y. Liu, Y. S. Wan, S. W. Liu, and J. H. Guo, 2006. Zircon geochronology and metamorphic evolution of mafic dykes in the Hengshan Complex of northern China: Evidence for late Palaeoproterozoic extension and subsequent high-pressure metamorphism in the North China Craton. ***Precambrian Research***, 146(1-2): 45-67.

Labaune, C., Tesson, M. and Gensous, B., 2008. Variability of the transgressive stacking pattern under environmental changes control: Example from the Post-Glacial deposits of the Gulf of Lions inner-shelf, Mediterranean, France. ***Continental Shelf Research***, 28(9): 1138-1152.

Lan, C., Yang, M. and Zhang, Y., 2016. Impact of sequence stratigraphy, depositional facies and diagenesis on reservoir quality: A case study on the Pennsylvanian Taiyuan sandstones, northeastern Ordos Basin, China. ***Marine and Petroleum Geology***, 69: 216-230.

881 Li, S., Wilde, S.A., Wang, T. and Guo, Q., 2013. Incremental growth and origin of the
882 Cretaceous Renjiayingzi pluton, southern Inner Mongolia, China: Evidence from structure,
883 geochemistry and geochronology. ***Journal of Asian Earth Sciences***, 75: 226-242.

884 Li, Z., Dong, S. and Qu, H., 2014. Timing of the initiation of the Jurassic Yanshan movement
885 on the North China Craton: Evidence from sedimentary cycles, heavy minerals, geochemistry,
886 and zircon U–Pb geochronology. ***International Geology Review***, 56(3): 288-312.

887 Liu, R., H. Xiao, L. Fan, C. Zhang, A. Hao, and W. Miao, 2013. A depositional mode of flood-
888 induced braided river delta in Permian of Ordos Basin. ***Acta Petrolei Sinica, with English***
889 ***Abstract***, S1(34): 120-127.

890 Liu, F., H. Zhu, and S. Ouyang, 2015, Late Pennsylvanian to Wuchiapingian
891 palynostratigraphy of the Baode section in the Ordos Basin, North China: ***Journal of Asian Earth***
892 ***Sciences***, 111: 528-552.

893 Martins-Neto, M.A., Pedrosa-Soares, A.C. and Lima, S.A.D.A., 2001. Tectono-sedimentary
894 evolution of sedimentary basins from Late Paleoproterozoic to Late Neoproterozoic in the Sao
895 Francisco craton and Araçuaı fold belt, eastern Brazil. ***Sedimentary Geology***, 141: 343-370.

896 McLaughlin, P.I., Brett, C.E., Taha McLaughlin, S.L. and Cornell, S.R., 2004. High-resolution
897 sequence stratigraphy of a mixed carbonate-siliciclastic, cratonic ramp (Upper Ordovician;
898 Kentucky–Ohio, USA): insights into the relative influence of eustasy and tectonics through
899 analysis of facies gradients. ***Palaeogeography, Palaeoclimatology, Palaeoecology***, 210(2-4):
900 267-294.

901 McLennan, S.M., Taylor, S.R., McCulloch, M.T. and Maynard, J.B., 1990. Geochemical and
902 Nd-Sr isotopic composition of deep-sea turbidites: Crustal evolution and plate tectonic

903 associations. ***Geochimica et Cosmochimica Acta***, 54(7): 2015-2050.

904 Michael, N.A., Whittaker, A.C. and Allen, P.A., 2013. The Functioning of Sediment Routing
905 Systems Using a Mass Balance Approach: Example from the Eocene of the Southern Pyrenees.
906 ***The Journal of Geology***, 121(6): 581-606.

907 Milne, G.A., Gehrels, W.R., Hughes, C.W. and Tamisiea, M.E., 2009. Identifying the causes of
908 sea-level change. ***Nature Geoscience***, 2(7): 471-478.

909 Montanez, I. P., N. J. Tabor, D. Niemeier, W. A. Dimichele, T. D. Frank, C. R. Fielding, J. L.
910 Isbell, L. P. Birgenheier, and M. C. Rygel, 2007. CO2-forced climate and vegetation instability
911 during Late Paleozoic deglaciation. ***Science***, 315(5808): 87-91.

912 Morton, A.C. and Hallsworth, C., 1994. Identifying provenance-specific features of detrital
913 heavy mineral assemblages in sandstones. ***Sedimentary Geology***, 90(3): 241-256.

914 Nikishin, A. M., P. A. Ziegler, R. A. Stephenson, S. A. P. L. Cloetingh, A. V. Furne, P. A. Fokin,
915 A. V. Ershov, S. N. Bolotov, M. V. Korotaev, A. S. Alekseev, V. I. Gorbachev, E. V. Shipilov, A.
916 Lankreijer, E. Y. Bembinova, and I. V. Shalimov, 1996. Late Precambrian to Triassic history of the
917 East European Craton: dynamics of sedimentary basin evolution. ***Tectonophysics***, 268(1): 23-63.

918 Pfefferkorn, H.W. and Wang, J., 2007. Early Permian coal-forming floras preserved as
919 compressions from the Wuda District (Inner Mongolia, China). International ***Journal of Coal***
920 ***Geology***, 69(1-2): 90-102.

921 Phillips, T.L. and Galtier, J., 2005. Evolutionary and ecological perspectives of Late Paleozoic
922 ferns Part I. Zygopteridales. ***Review of Palaeobotany and Palynology***, 135(3-4): 165-203.

923 Phillips, T.L. and Galtier, J., 2011. Evolutionary and ecological perspectives of late Paleozoic
924 ferns Part II. The genus Ankyropteris and the Tedeleaceae. ***Review of Palaeobotany and***

925 ***Palynology***, 164(1-2): 1-29.

926 Pratt, L.M., Phillips, T.L. and Dennison, J.M., 1978. Evidence of non-vascular land plants from
927 the Early Silurian (Llandoverian) of Virginia, USA. ***Review of palaeobotany and palynology***,
928 25(2): 121-149.

929 Pu, R., Zhu, L. and Zhong, H., 2009. 3-D seismic identification and characterization of ancient
930 channel morphology. Journal of Earth Science, 20(5): 858-867.

931 Qin, C., 2002. The thickness of seismogenic layer under the areas surrounding the Ordos
932 block, Northern China. ***Pure and Applied Geophysics***, 159(11-12): 2613-2628.

933 Qiu, X., C. Liu, G. Mao, Y. Deng, F. Wang, and J. Wang, 2015a. Major, trace and platinum-
934 group element geochemistry of the Upper Triassic nonmarine hot shales in the Ordos basin,
935 Central China. ***Applied Geochemistry***, 53: 42-52.

936 Qiu, X., Liu, C., Wang, F., Deng, Y. and Mao, G., 2015b. Trace and rare earth element
937 geochemistry of the Upper Triassic mudstones in the southern Ordos Basin, Central China.
938 ***Geological Journal***, 50(4): 399-413.

939 Raucsik, B. and Varga, A., 2008. Climato-environmental controls on clay mineralogy of the
940 Hettangian–Bajocian successions of the Mecsek Mountains, Hungary: An evidence for extreme
941 continental weathering during the early Toarcian oceanic anoxic event. ***Palaeogeography,***
942 ***Palaeoclimatology, Palaeoecology***, 265(1-2): 1-13.

943 Ren, Z., S. Zhang, S. Gao, J. Cui, Y. Xiao, and H. Xiao, 2007, Tectonic thermal history and its
944 significance on the formation of oil and gas accumulation and mineral deposit in Ordos Basin:
945 ***Science in China Series D: Earth Sciences***, 50(S2): 27-38.

946 Rimmer, S.M., 2004. Geochemical paleoredox indicators in Devonian–Mississippian black

947 shales, Central Appalachian Basin (USA). ***Chemical Geology***, 206(3-4): 373-391.

948 Ritts, B.D., Keele, D., Darby, B.J. and Liu, S., 2006. Ordos Basin Gas Reservoir Outcrop
949 Analogs: Permian Braided Fluvial Sandstone of the Zhuozi Shan and Helan Shan, China.
950 ***International Geology Review***, 48(7): 573-584.

951 Ruppen, D. et al., 2014. Restoring the Silurian to Carboniferous northern active continental
952 margin of the Mongol–Okhotsk Ocean in Mongolia: Hangay–Hentey accretionary wedge and
953 seamount collision. ***Gondwana Research***, 25(4): 1517-1534.

954 Shen, Y., Y. Qin, G. G. X. Wang, Y. Guo, J. Shen, J. Gu, Q. Xiao, T. Zhang, C. Zhang, and G.
955 Tong, 2017. Sedimentary control on the formation of a multi-superimposed gas system in the
956 development of key layers in the sequence framework. ***Marine and Petroleum Geology***, 88:
957 268-281.

958 Shi, J., Wenhui, H., Chenhang, L. and Xiaonan, C., 2018. Geochemical characteristics and
959 geological significance of the Upper Paleozoic mudstones from Linxing area in Ordos Basin. ***Acta***
960 ***Petrolei sinica, with English abstract***, 8(39): 876-889.

961 Shi, J., Zeng, L., Zhao, X., Zhang, Y. and Wang, J., 2020. Characteristics of natural fractures
962 in the upper Paleozoic coal-bearing strata in the southern Qinshui Basin, China: Implications for
963 coalbed methane (CBM) development. ***Marine and Petroleum Geology***, 113: 104152.

964 Sloss, L.L., 1963. Sequences in the cratonic interior of North America. ***Geological Society of***
965 ***America Bulletin***, 74(2): 93-114.

966 Song, S., Su, L., Li, X., Niu, Y. and Zhang, L., 2012. Grenville-age orogenesis in the Qaidam-
967 Qilian block: The link between South China and Tarim. ***Precambrian Research***, 220-221: 9-22.

968 Stanley, S.M. and Powell, M.G., 2003. Depressed rates of origination and extinction during the

969 late Paleozoic ice age: A new state for the global marine ecosystem. ***Geology***, 31(10): 877.

970 Stollhofen, H., Stanistreet, I.G., Bangert, B. and Grill, H., 2000. Tuffs, tectonism and glacially
971 related sea-level changes, Carboniferous–Permian, southern Namibia. ***Palaeogeography,***
972 ***Palaeoclimatology, Palaeoecology***, 161(1-2): 127-150.

973 Sun, B., Zeng, F., Liu, C., Cui, X. and Wang, W., 2014. Constraints on U-Pb Dating of Detrial
974 Zircon of the Maximum Depositional Age for Upper Paleozoic Coal-Bearing Strata in Xishan,
975 Taiyuan and Its Stratigraphic Significance. ***Acta Geologica sinica-English Abstract***, 2(88): 185-
976 197.

977 Syvitski, J.P.M. and Milliman, J.D., 2007. Geology, Geography, and Humans Battle for
978 Dominance over the Delivery of Fluvial Sediment to the Coastal Ocean. ***The Journal of Geology***,
979 115(1): 1-19.

980 Tabor, N.J. and Poulsen, C.J., 2008. Palaeoclimate across the Late Pennsylvanian–Early
981 Permian tropical palaeolatitudes: A review of climate indicators, their distribution, and relation to
982 palaeophysiographic climate factors. ***Palaeogeography, Palaeoclimatology, Palaeoecology***,
983 268(3-4): 293-310.

984 Teipel, U., R. Eichhorn, G. Loth, J. Rohrmüller, R. Höll, and A. Kennedy, 2004, U-Pb SHRIMP
985 and Nd isotopic data from the western Bohemian Massif (Bayerischer Wald, Germany):
986 implications for upper Vendian and lower Ordovician magmatism: ***International Journal of Earth***
987 ***Sciences***, 93(5): 782-801.

988 Wang, A. Q., D. B. Yang, H. T. Yang, M. S. Mu, Y. K. Quan, L. R. Hao, and W. L. Xu, 2019.
989 Late Palaeozoic tectonic evolution of the southern North China Craton: Constraints from detrital
990 zircon dating and Hf–O isotopic compositions of the Benxi Formation, Sanmenxia area, North

China Craton. ***Geological Journal***, 55(2): 1320-1331.

Wang, J., 2010. Late Paleozoic macrofloral assemblages from Weibei Coalfield, with reference to vegetational change through the Late Paleozoic Ice-age in the North China Block. ***International Journal of Coal Geology***, 83(2-3): 292-317.

Wang, J., Feng, Z., Zhang, Y. and Wang, S., 2009. Confirmation of Sigillaria Brongniart as a coal-forming plant in Cathaysia: occurrence from an Early Permian autochthonous peat-forming flora in Inner Mongolia. ***Geological Journal***, 44(4): 480-493.

Wang, Y., H. Li, L. Gu, C. Wu, D. Chai, P. Chen, S. Wang, and J. Zhang, 2003, Rb-Sr istope dating bauxite deposits in Shanxi Province: ***Acta Geoscientica Sinica, with English abstract***, 6(24): 589-592.

Xie, X. and Heller, P.L., 2013. U-Pb detrital zircon geochronology and its implications: The early Late Triassic Yanchang Formation, south Ordos Basin, China. ***Journal of Asian Earth Sciences***, 64: 86-98.

Xin, S., Y. Xinghe, P. Clift, L. Yalong, J. Lina, S. Dongxu, Y. DU, Z. Jinsong, and H. Xiaoqin, 2018. Sedimentology and Sequence Stratigraphy of Marine to Lacustrine Deltaic Deposits in a Craton Basin and Their Controlling Factors: Shan 2 Member-He 8 Member (Guadalupian-Lopingian, Permian), Southeast Ordos Basin, North China. ***Acta Geologica Sina-English Edition***, 92(1): 268-285.

Xu, H., D. Tang, S. Tang, W. Zhang, Y. Meng, L. Gao, S. Xie, and J. Zhao, 2015. Geologic and hydrological controls on coal reservoir water production in marine coal-bearing strata: A case study of the Carboniferous Taiyuan Formation in the Liulin area, eastern Ordos Basin, China. ***Marine and Petroleum Geology***, 59: 517-526.

1013 Xu, Q., W. Shi, X. Xie, W. Manger, P. McGuire, X. Zhang, R. Wang, and Z. Xu, 2016. Deep-
1014 lacustrine sandy debrites and turbidites in the lower Triassic Yanchang Formation, southeast
1015 Ordos Basin, central China: Facies distribution and reservoir quality. ***Marine and Petroleum***
1016 ***Geology***, 77: 1095-1107.

1017

1018 Yang, H., Fu, J., Wei, X. and Liu, X., 2008. Sulige field in the Ordos Basin: Geological setting,
1019 field discovery and tight gas reservoirs. ***Marine and Petroleum Geology***, 25(4-5): 387-400.

1020 Yang, R., Fan, A., Han, Z. and van Loon, A.J.T., 2017. Lithofacies and origin of the Late
1021 Triassic muddy gravity-flow deposits in the Ordos Basin, central China. ***Marine and Petroleum***
1022 ***Geology,*** 85: 194-219.

1023 Yang, Y., Li, W. and Ma, L., 2005. Tectonic and stratigraphic controls of hydrocarbon systems
1024 in the Ordos basin: A multicycle cratonic basin in central China. ***AAPG bulletin***, 89(2): 255-269.

1025 Yin, S., Tian, T. and Wu, Z., 2019. Developmental characteristics and distribution law of
1026 fractures in a tight sandstone reservoir in a low-amplitude tectonic zone, eastern Ordos Basin,
1027 China. ***Geological Journal***, 55(2): 1546-1562.

1028 Yu, Q., Z. Ren, B. Wang, L. Gao, C. Li, and H. Cao, 2012, Thermal Evolution History of the
1029 Upper Paleozoic in Yanchang Exploratory Area, Ordos Basin: ***Geological Review, with English***
1030 ***abstract,*** 58(2): 303-308.

1031 Yuan, Y., S. Hu, H. Wang, and F. Sun, 2007, Meso-Cenozoic tectonothermal evolution of
1032 Ordos basin, central China: Insights from newly acquired vitrinite reflectance data and a revision
1033 of existing paleothermal indicator data: ***Journal of Geodynamics***, 44(1-2): 33-46.

1034 Zecchin, M., L. Baradello, G. Brancolini, F. Donda, F. Rizzetto, and L. Tosi, 2008. Sequence

1035 stratigraphy based on high-resolution seismic profiles in the late Pleistocene and Holocene
1036 deposits of the Venice area. ***Marine Geology***, 253(3-4): 185-198.

1037 Zhang, L., Bai, G., Luo, X., Ma, X., Chen, M., & Wu, M., et al. (2009). Diagenetic history of
1038 tight sandstones and gas entrapment in the Yulin Gas Field in the central area of the Ordos Basin,
1039 China. ***Marine and Petroleum Geology***, 26(6), 974-989.

1040 Zhang, L., Sun, M., Wang, S. and Yu, X., 1998. The composition of shales from the Ordos
1041 basin, China: effects of source weathering and diagenesis. ***Sedimentary Geolog***y, 116(1-2):
1042 129-141.

1043 Zhang, Z., Sun, K. and Yin, J., 1997. Sedimentology and sequence stratigraphy of the Shanxi
1044 Formation (Lower Permian) in the northwestern Ordos Basin, China: an alternative sequence
1045 model for fluvial strata. ***Sedimentary Geology***, 112(1): 123-136.

1046 Zhang, D., Yang, W., Qi, Y. and Yan, X., 2009. Analysis of the Material Source of Upper
1047 Paleozoic Shanxi Formation in Shenmu Region of Ordos basin. ***Natural Gas Geoscience, with***
1048 ***English Abstract***, 20(6): 901-906.

1049 Zhu, H., Chen, K., Liu, K. and He, S., 2008. A sequence stratigraphic model for reservoir sand-
1050 body distribution in the Lower Permian Shanxi Formation in the Ordos Basin, northern China.
1051 ***Marine and Petroleum Geology***, 25(8): 731-743.

1052 Zhu, X., F. Chen, S. Li, Y. Yang, H. Nie, W. Siebel, and M. Zhai, 2011. Crustal evolution of the
1053 North Qinling terrain of the Qinling Orogen, China: Evidence from detrital zircon U–Pb ages and
1054 Hf isotopic composition. ***Gondwana Research***, 20(1): 194-204.

1055 Zou, C.N. et al., 2013. Continuous hydrocarbon accumulation over a large area as a
1056 distinguishing characteristic of unconventional petroleum: The Ordos Basin, North-Central China.

1057 ***Earth-Science Reviews***, 126: 358-369.

TABLE 1

Facies Association	***Lithofacies***	***Main sedimentary features***	***Inferred depositional environment***
LFA.1	*Sp-Sm-M*	Moderately to well sorting thick sandstone. There are thick bad association trough crossing bedding. The thin layer of mudstone observed in the top.	Slow-rate flow deposited (Meandering channel environment) (refer to *Blum and Törnqvist (2000)*)
LFA.2	*Sb-Scm(Scc)-M*	Moderately sorted homogeneous sandstone. Regularly lamellar crossing bedding in the top.	High-rate traction flow deposited (Braid channel environment)
LFA.3	*Sb-Scm-Scc-M*	Strong rhythmic alteration of darker or lighter layers composed of fine-grained slit stone. The double-clay cross-bedding in the upper part.	Bidirectional slow-rate traction flow deposit(Tidal environment)
LFA.4	*Gp-Sd-Gm*	Gravel-supported conglomerate with regular imbedded layers. Upper to the top, matrix-supported conglomerate shows an imbricated orientation	A static water setting (Swamp)(refer to *Ichaso and Dalrymple (2009)*)
LFA.5	*Sd-Scc-M*	Moderately sorted fine stone in the bottom. Deformation structure occurs in the laminae. Despite intense bioturbation, there is no single trace identified.	Interchannel environment
LFA.6	-	Homogeneous carbonate with some mud clast identified in the top	Carbonate plate environment

TABLE.2

Period	Potential Source Area	Zircon	Tourmaline	Rutile	Titanite	Garnet	Ilmenite	Apatite	Pyroxene	Pyrite	Spinel	Types of heavy mineral assemblage	References
Pennsylvanian	Yishan Orogenic belt	28.25	28.96	9.28	12.00			10.08			3.36	HMA-I Rutile dominated	Chen et al., 2009
Pennsylvanian	Qaidam–Qilian orogenic belt	9.08	0.04	0.15	0.01			7.96		58.6		HMA-II Pyrite dominated	Du et al., 2017
Early Premarin	Yishan Orogenic belt	20.91	1.93	11.25	30.00			7.96				HMA-IIITitanite dominated	Ruppen et al., 2014; Li et al., 2014
Early Permian	Yishan Orogenic belt	10.96	36.15	3.94	7.02			0.99				HMA-IV Tourmaline dominated	Xin et al. 2018
Early Permian	Qiling orogenic belt	43.42	5.74	11.48	16.86		0.12		0.12		0.12	HMA-V Zircon dominated	Zhang et al., 2009

TABLE 3

Fm.	*Block*	*Ave. Dip Angle*	*Provenance Area*	*Sink Area*	*Pathway Cut Area/km^2*	*Uplift Evaluated Height*	*Average Transgression/Regression Rate*
Penzi Formation	*T.P.1*	*0.74*	*11.13*	*10.09*	*9.78*	*76.13*	*13.50*
	T.P.2	*0.94*	*11.54*	*12.86*	*7.36*	*73.23*	*14.09*
	T.P.3	*0.75*	*8.92*	*12.87*	*8.48*	*75.03*	*14.89*
	T.P.4	*0.86*	*11.60*	*11.82*	*5.70*	*70.74*	*14.45*
	R.P.1	*0.80*	*8.93*	*16.68*	*6.80*	*74.57*	*15.80*
	R.P.2	*0.71*	*7.68*	*16.24*	*6.90*	*72.18*	*13.40*
	R.P.3	*0.87*	*9.98*	*9.27*	*7.04*	*72.76*	*16.36*
Taiyuan Formation	*T.P.4*	*0.81*	*11.94*	*12.14*	*8.72*	*53.36*	*17.96*
	T.P.5	*0.97*	*16.24*	*16.68*	*8.76*	*53.10*	*13.17*
Lower Shanxi Formation	*T.P.6*	*0.79*	*20.90*	*21.49*	*7.12*	*73.18*	*44.10*
	R.P.4	*0.68*	*26.53*	*26.34*	*7.34*	*72.54*	*53.06*
Upper Shanxi Formation	*R.P.5*	*0.83*	*11.24*	*10.21*	*8.46*	*80.35*	*25.04*
	R.P.6	*0.88*	*16.30*	*16.91*	*7.20*	*84.20*	*37.73*
	T.P.7	*0.97*	*22.05*	*20.28*	*6.78*	*79.57*	*32.20*
Penzi Formation	*T.P.8*	*0.84*	*8.26*	*17.38*	*8.24*	*77.08*	*17.32*
	T.P.9	*0.94*	*8.53*	*8.25*	*6.84*	*70.83*	*16.55*
	T.P.10	*0.89*	*8.67*	*9.50*	*10.44*	*78.00*	*16.72*
	R.P.7	*0.69*	*9.88*	*10.23*	*7.28*	*70.93*	*23.86*
	R.P.8	*0.94*	*8.75*	*8.59*	*7.04*	*75.81*	*15.12*
Taiyuan Formation	*T.P.11*	*0.87*	*15.76*	*16.18*	*9.02*	*53.17*	*19.88*
	T.P.12	*0.84*	*10.33*	*8.33*	*8.56*	*53.10*	*19.82*
Lower Shanxi Formation	*T.P.13*	*0.64*	*5.78*	*5.79*	*9.68*	*74.97*	*21.57*
	R.P.9	*0.67*	*5.42*	*6.46*	*7.30*	*72.19*	*27.41*
Upper Shanxi Formation	*R.P.10*	*0.58*	*6.16*	*5.14*	*6.34*	*84.91*	*37.71*

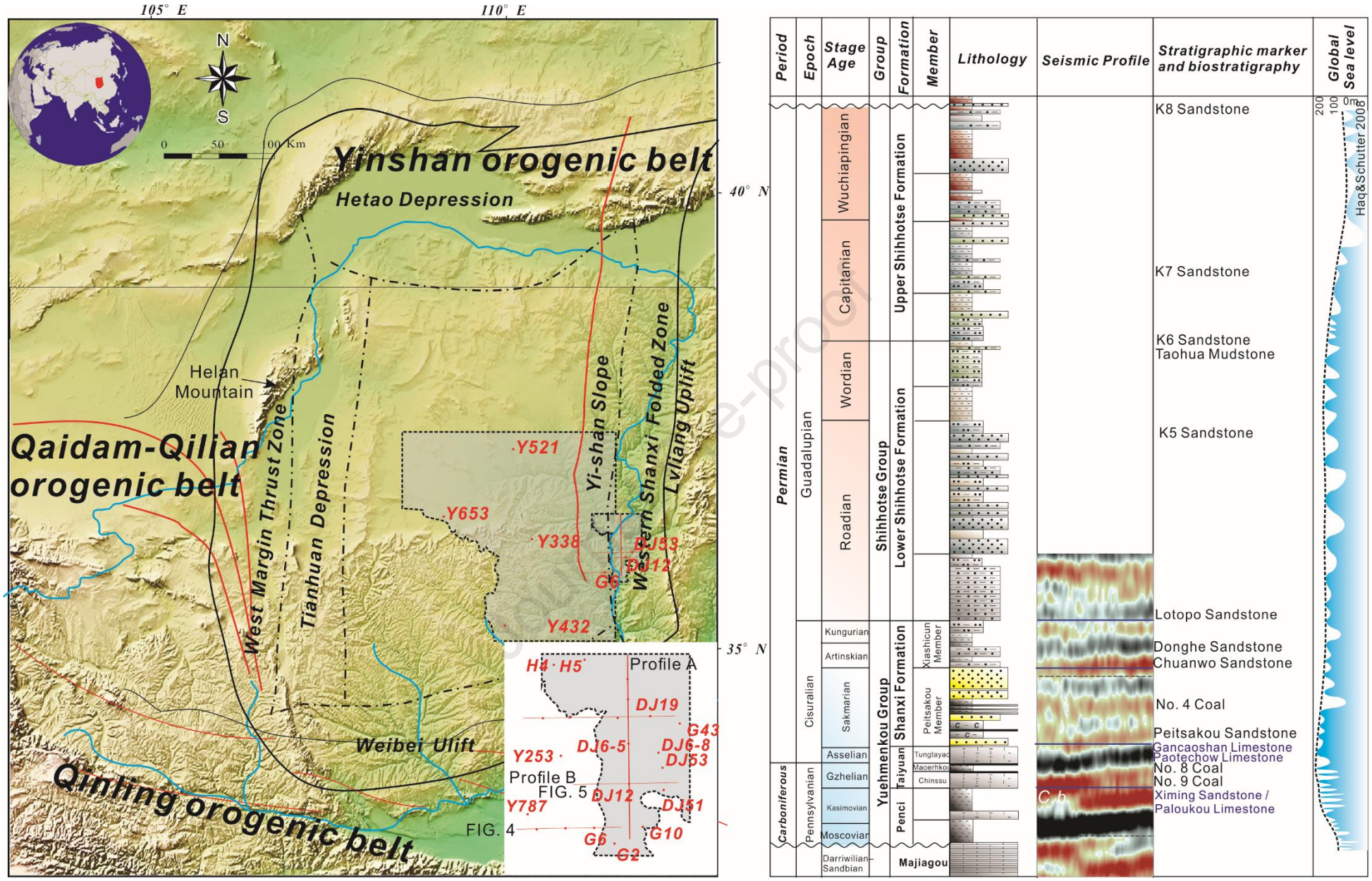
105° E
110° E
N
S
0 50 100 Km
Yinshan orogenic belt
Hetao Depression
40° N
Helan Mountain
Qaidam-Qilian orogenic belt
West Margin Thrust Zone
Tianhuan Depression
Yi-shan Slope
Western Shanxi Folded Zone
Lvliang Uplift
Y521
Y653
Y338
DJ53
DJ12
G6
Y432
35° N
Weibei Ulift
Qinling orogenic belt
H4
H5
Profile A
DJ19
G43
DJ6-5
DJ6-8
DJ53
Y253
Profile B
FIG. 5
DJ12
DJ51
Y787
FIG. 4
G10
G6
G2
Period
Epoch
Stage Age
Group
Formation
Member
Lithology
Seismic Profile
Stratigraphic marker and biostratigraphy
Global Sea level
Permian
Carboniferous
Guadalupian
Cisuralian
Pennsylvanian
Wuchiapingian
Capitanian
Wordian
Roadian
Kungurian
Artinskian
Sakmarian
Asselian
Gzhelian
Kasimovian
Moscovian
Darriwilian–Sandbian
Upper Shihhotse Formation
Shihhotse Group
Lower Shihhotse Formation
Yuehmenkou Group
Shanxi Formation
Taiyuan
Penci
Majiagou
Xiashicun Member
Peitsakou Member
Tungtayao
Maoerhkou
Chinssu
C b
K8 Sandstone
K7 Sandstone
K6 Sandstone
Taohua Mudstone
K5 Sandstone
Lotopo Sandstone
Donghe Sandstone
Chuanwo Sandstone
No. 4 Coal
Peitsakou Sandstone
Gancaoshan Limestone
Paotechow Limestone
No. 8 Coal
No. 9 Coal
Ximing Sandstone /
Paloukou Limestone
200
100
0m
Haq&Schutter 2008

FIG 1

FIG 2

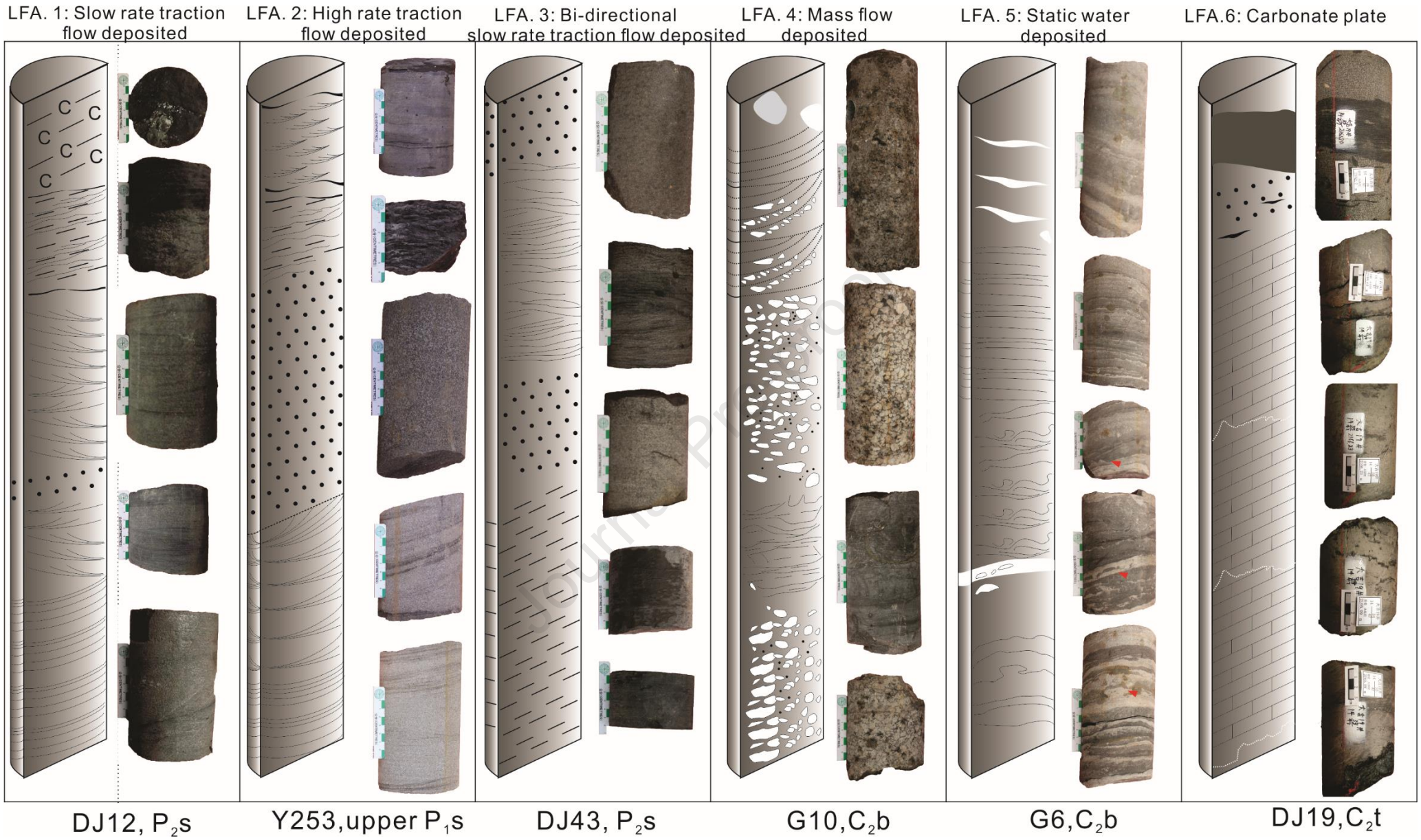
LFA. 1: Slow rate traction flow deposited
LFA. 2: High rate traction flow deposited
LFA. 3: Bi-directional slow rate traction flow deposited
LFA. 4: Mass flow deposited
LFA. 5: Static water deposited
LFA.6: Carbonate plate
DJ12, P2s
Y253,upper P1s
DJ43, P2s
G10,C2b
G6,C2b
DJ19,C2t

FIG 3

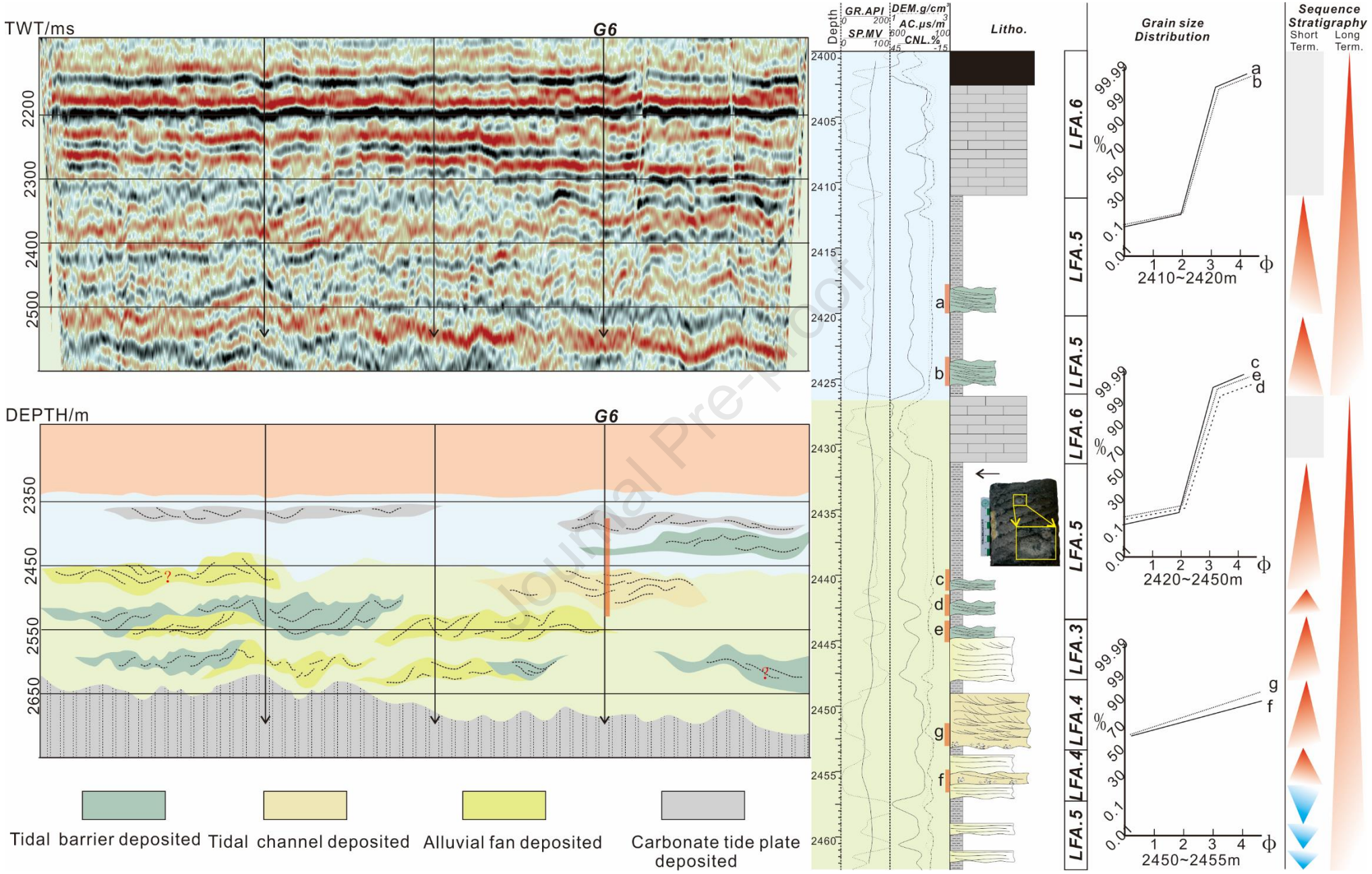

FIG 4

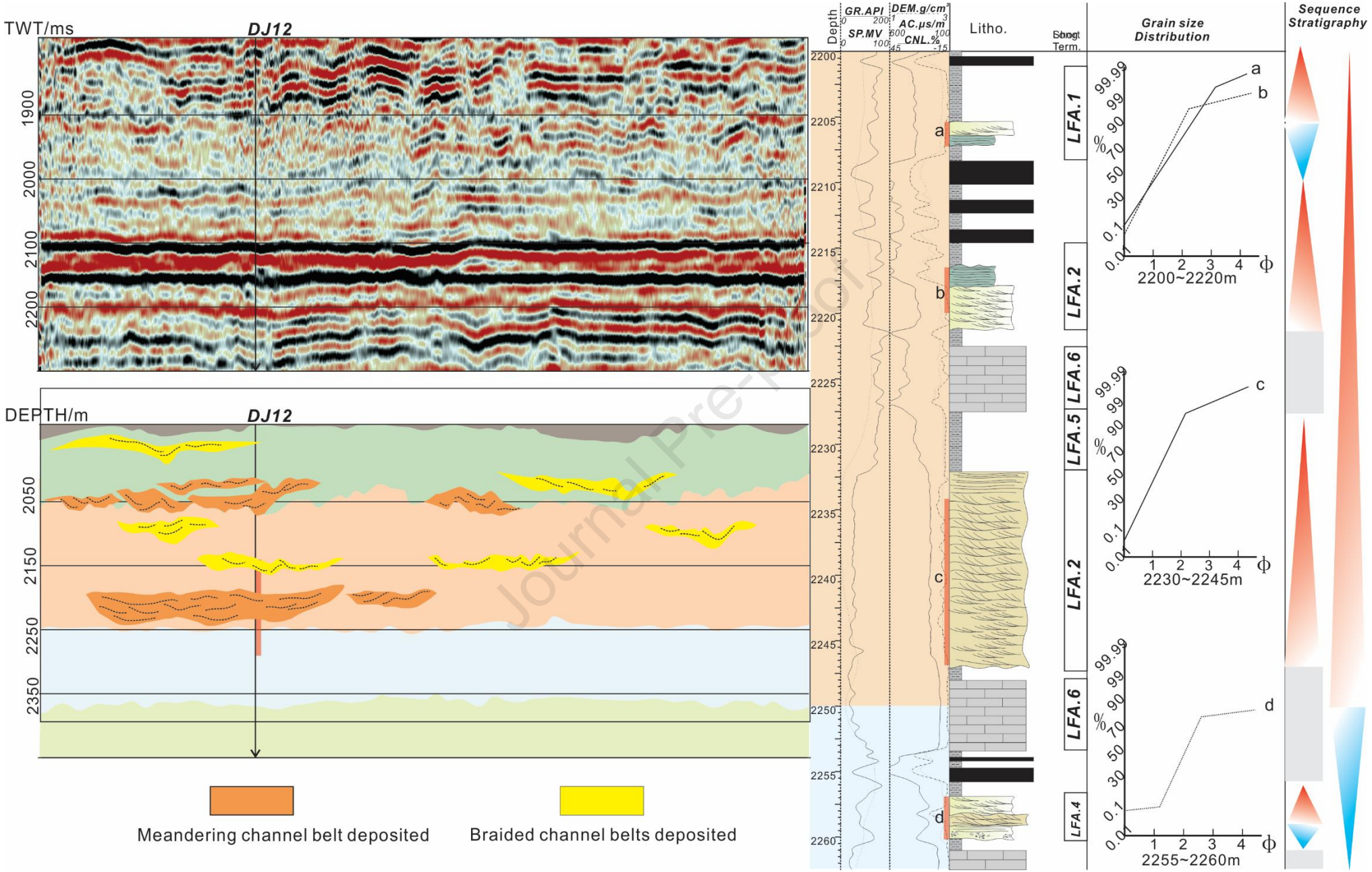
TWT/ms
DJ12
1900
2000
2100
2200
DEPTH/m
DJ12
2050
2150
2250
2350
Meandering channel belt deposited
Braided channel belts deposited
Depth
GR.API
SP.MV
DEM.g/cm³
AC.μs/m
CNL.%
Litho.
Strat. Term.
Grain size Distribution
Sequence Stratigraphy
LFA.1
LFA.2
LFA.6
LFA.5
LFA.2
LFA.6
LFA.4
2200~2220m
2230~2245m
2255~2260m

FIG 5

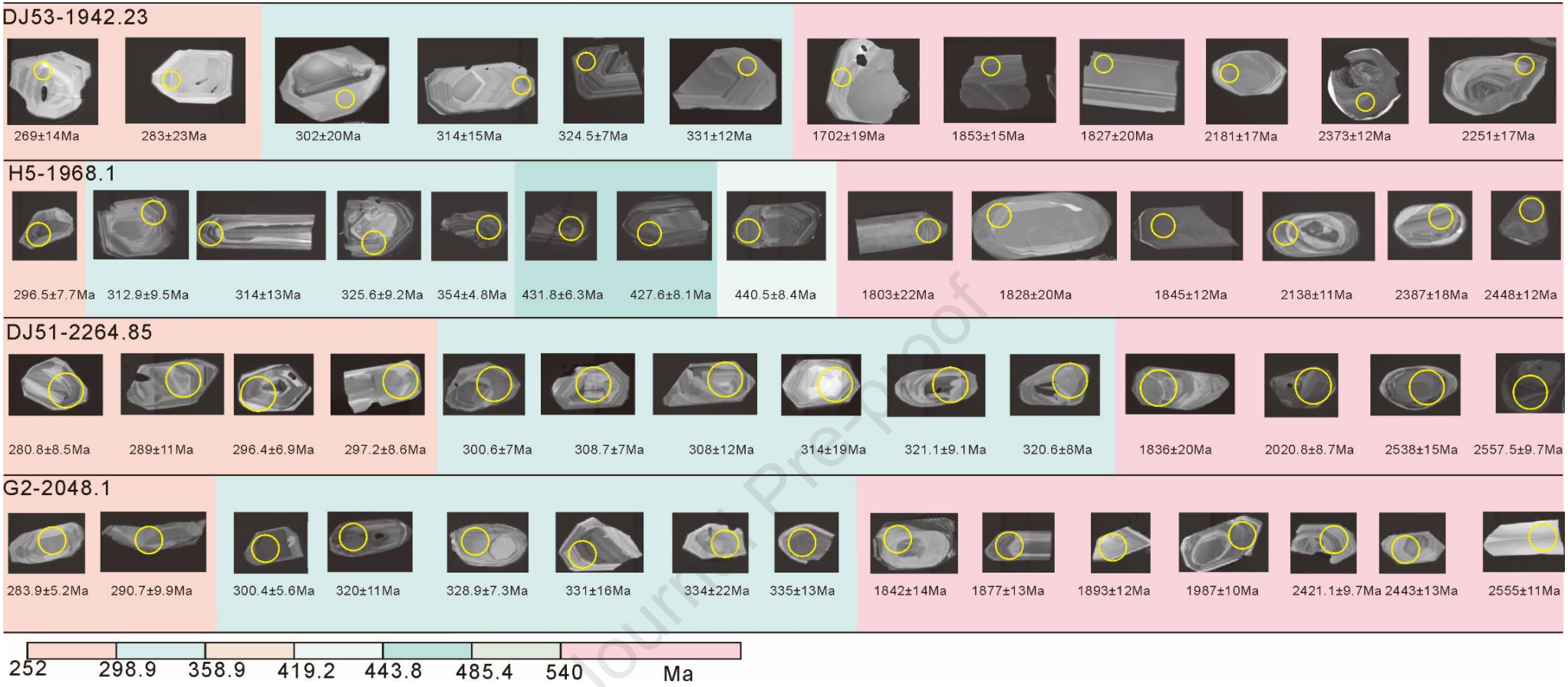

FIG 6

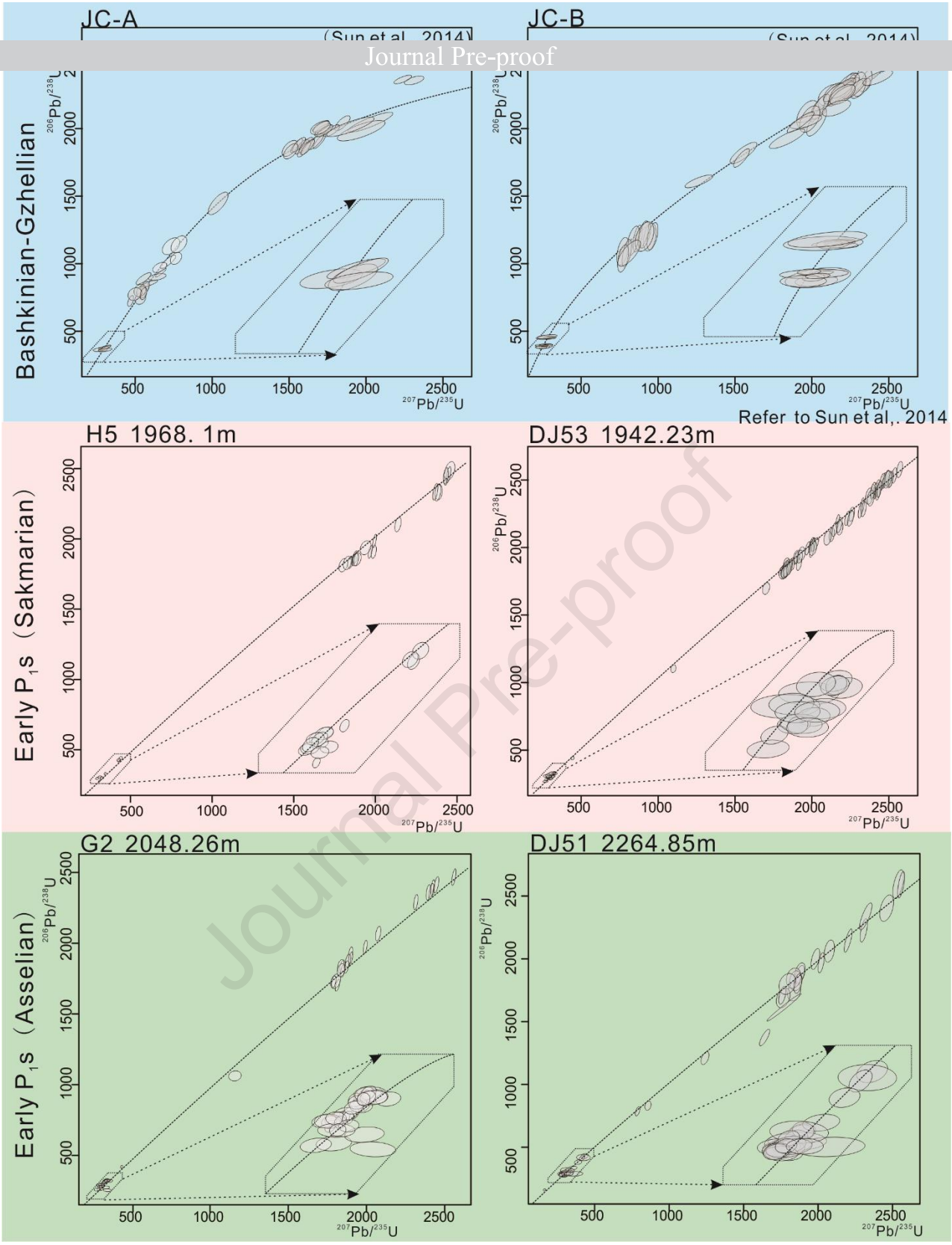

FIG 7

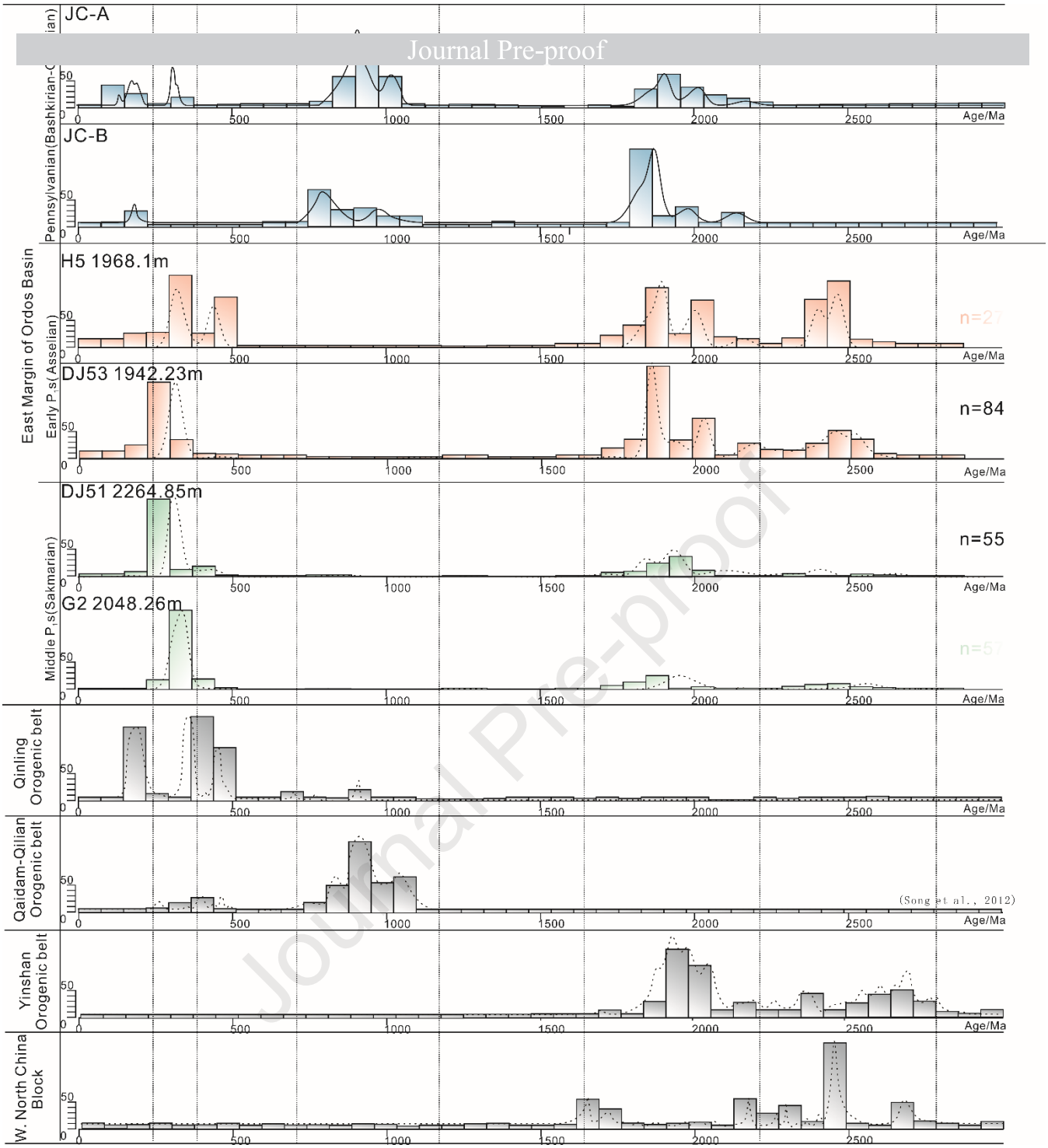

FIG 8

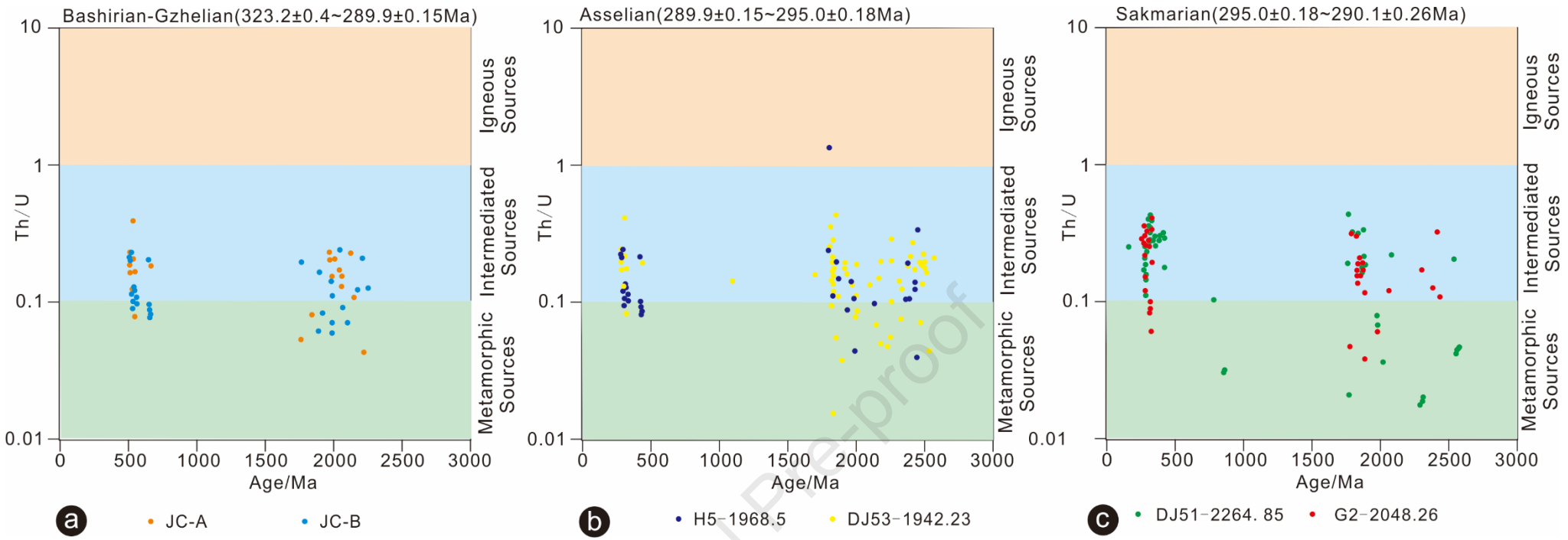

FIG 9

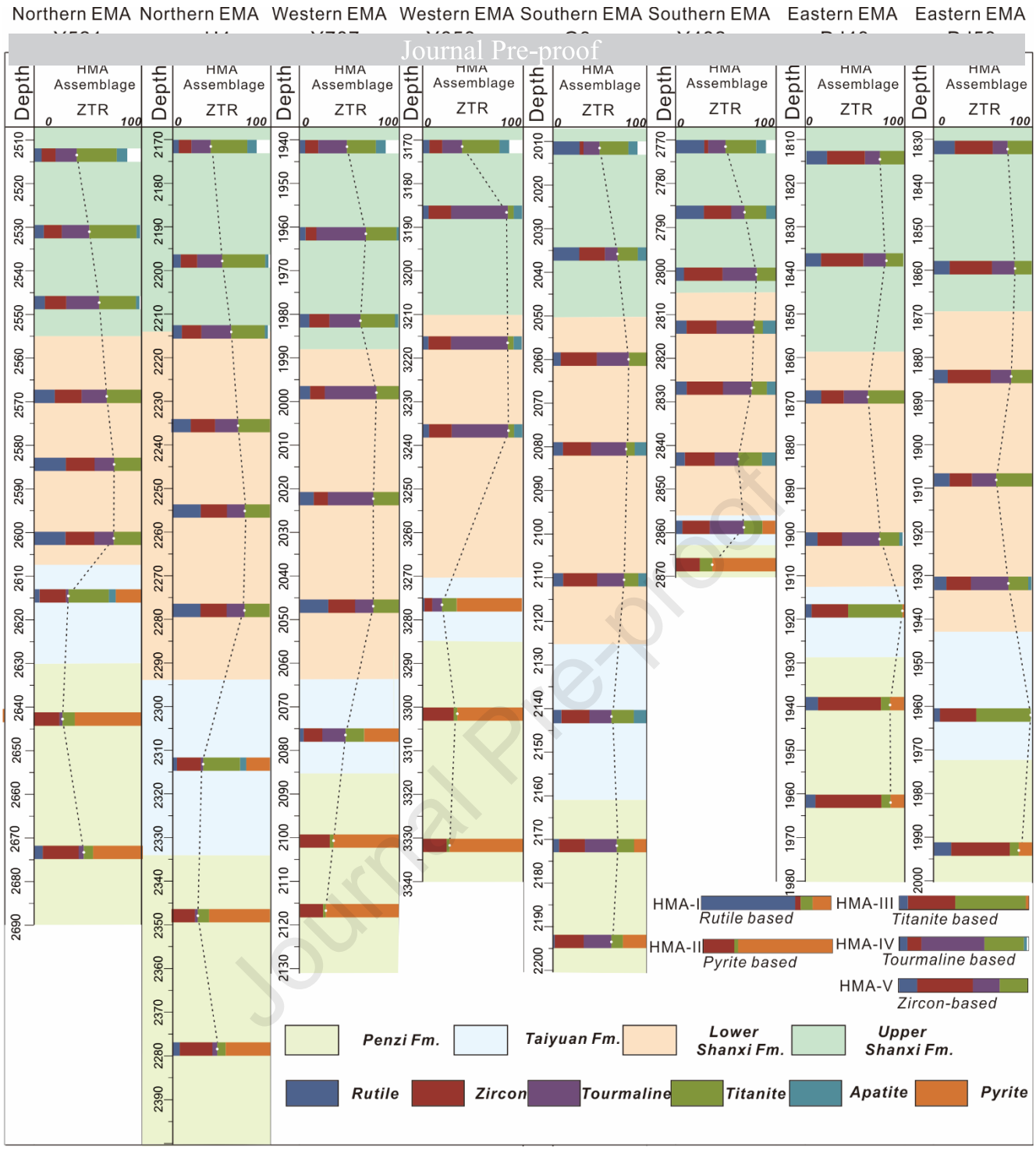

FIG 10

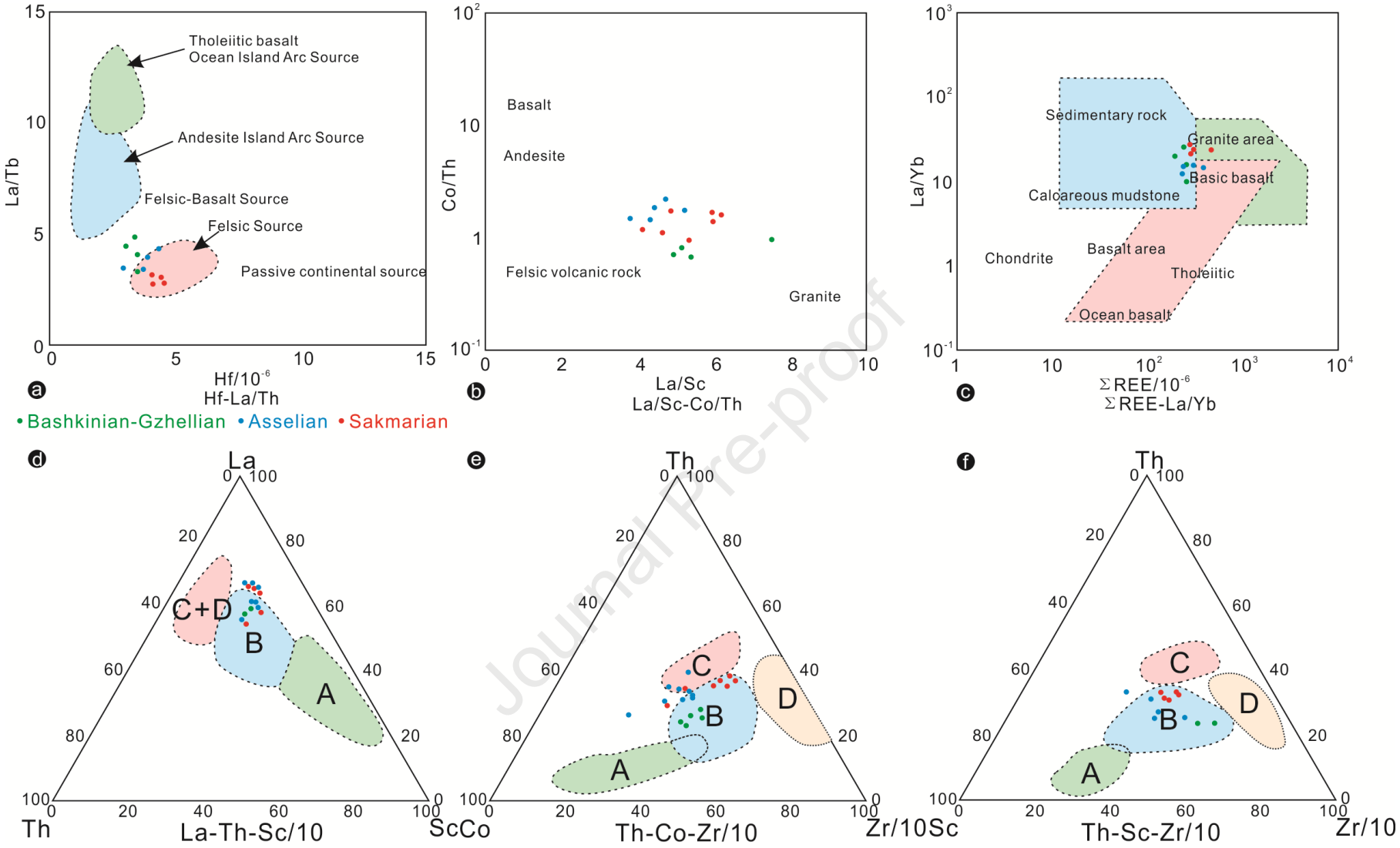

A-Continental island arc B-Ocean island arc C-Active continental margin D-Passive continental margin

FIG 11

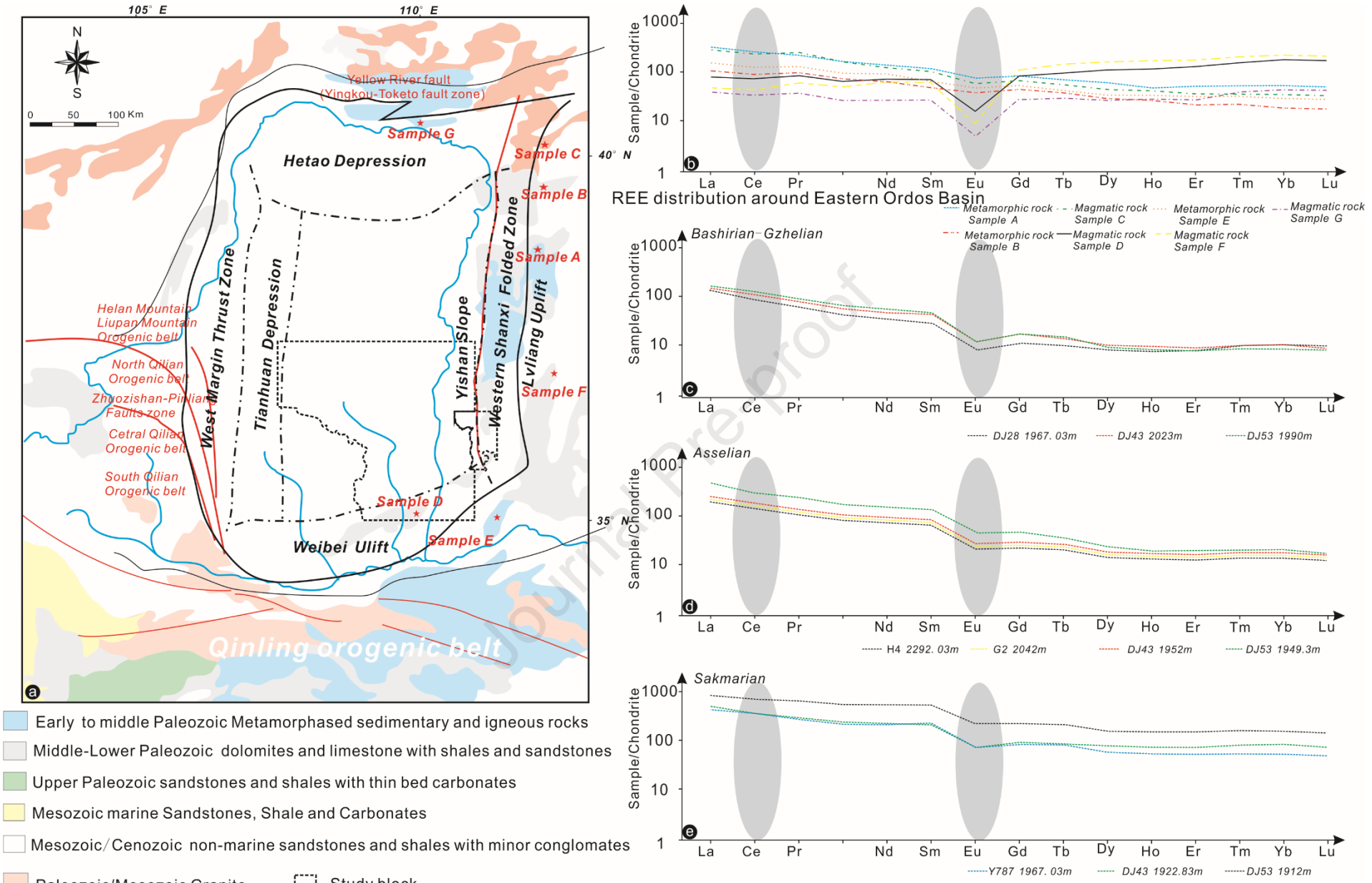
105° E
110° E
N
S
0 50 100 Km
Yellow River fault
(Yingkou-Toketo fault zone)
Sample G
Sample C
40° N
Sample B
Sample A
Sample F
Sample D
Sample E
35° N
Hetao Depression
Weibei Ulift
West Margin Thrust Zone
Tianhuan Depression
Yishan Slope
Western Shanxi Folded Zone
Lvliang Uplift
Helan Mountain
Liupan Mountain
Orogenic belt
North Qilian
Orogenic belt
Zhuozishan-Pingliang
Faults zone
Cetral Qilian
Orogenic belt
South Qilian
Orogenic belt
Qinling orogenic belt
a
Early to middle Paleozoic Metamorphased sedimentary and igneous rocks
Middle-Lower Paleozoic dolomites and limestone with shales and sandstones
Upper Paleozoic sandstones and shales with thin bed carbonates
Mesozoic marine Sandstones, Shale and Carbonates
Mesozoic/Cenozoic non-marine sandstones and shales with minor conglomates
Paleozoic/Mesozoic Granite
Study block
REE distribution around Eastern Ordos Basin
Sample/Chondrite
1000
100
10
1
La Ce Pr Nd Sm Eu Gd Tb Dy Ho Er Tm Yb Lu
b
Metamorphic rock Sample A
Magmatic rock Sample C
Metamorphic rock Sample E
Magmatic rock Sample G
Metamorphic rock Sample B
Magmatic rock Sample D
Magmatic rock Sample F
Bashirian-Gzhelian
c
DJ28 1967. 03m
DJ43 2023m
DJ53 1990m
Asselian
d
H4 2292. 03m
G2 2042m
DJ43 1952m
DJ53 1949.3m
Sakmarian
e
Y787 1967. 03m
DJ43 1922.83m
DJ53 1912m

FIG 12

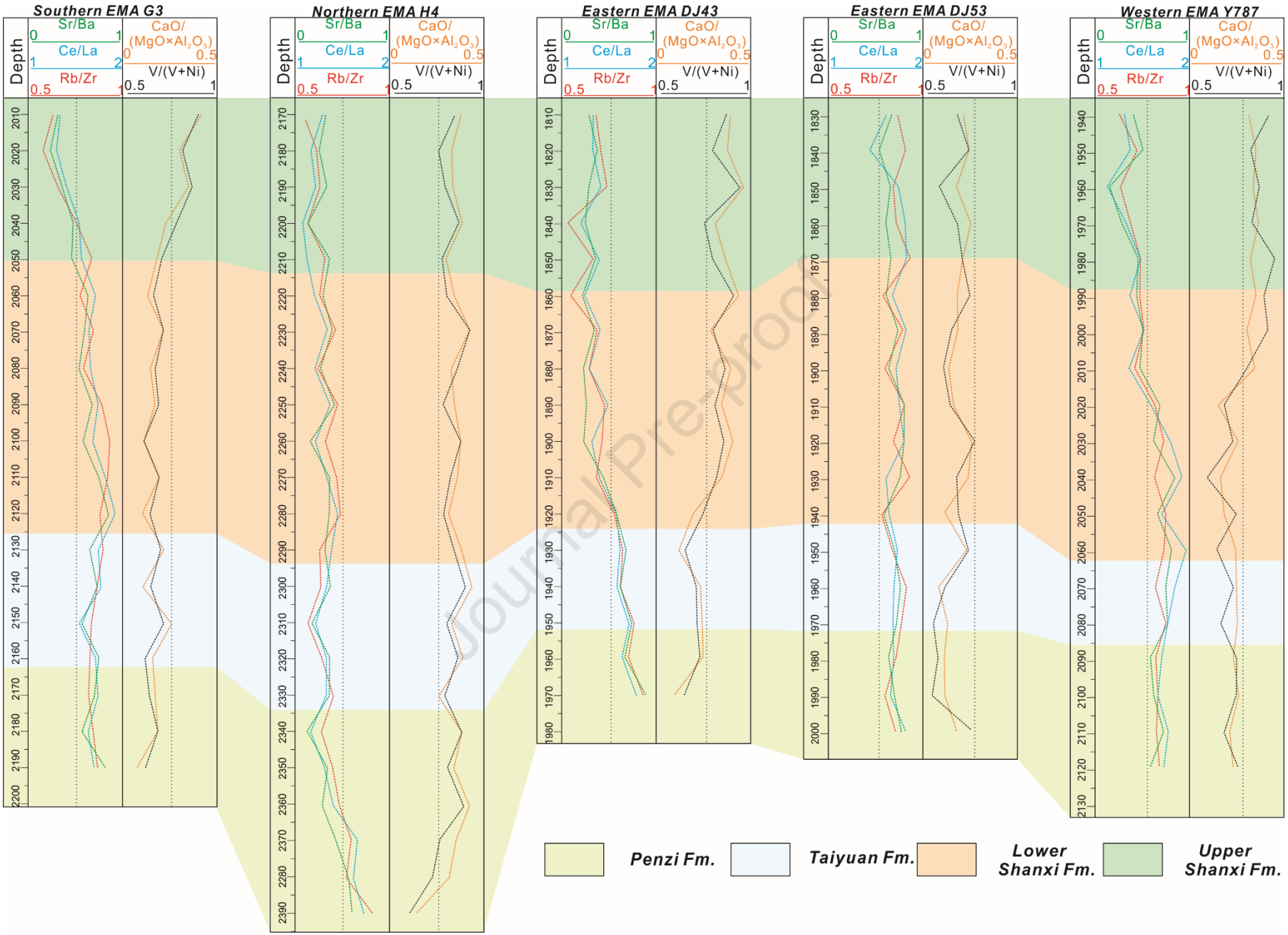

FIG 13

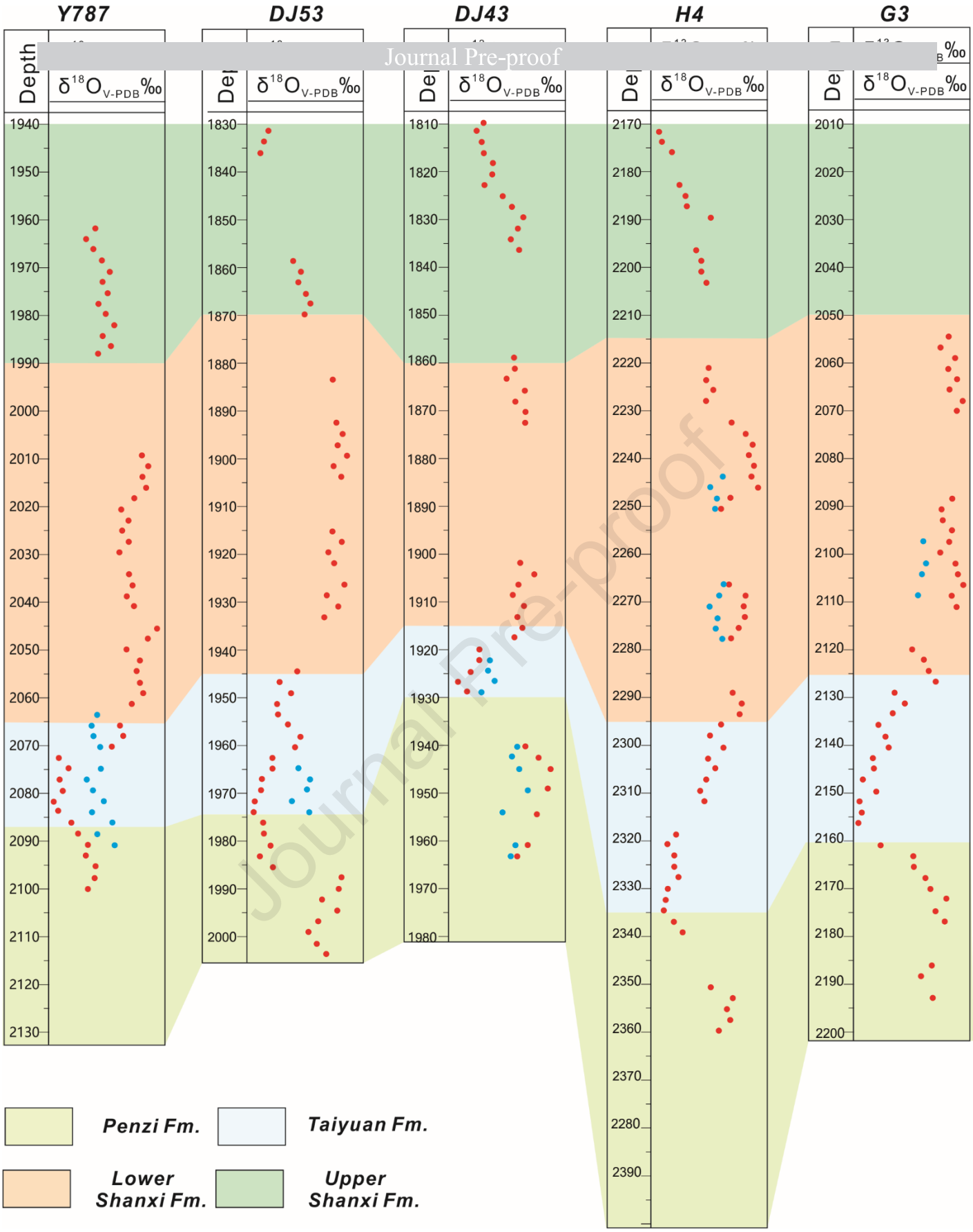

FIG 14

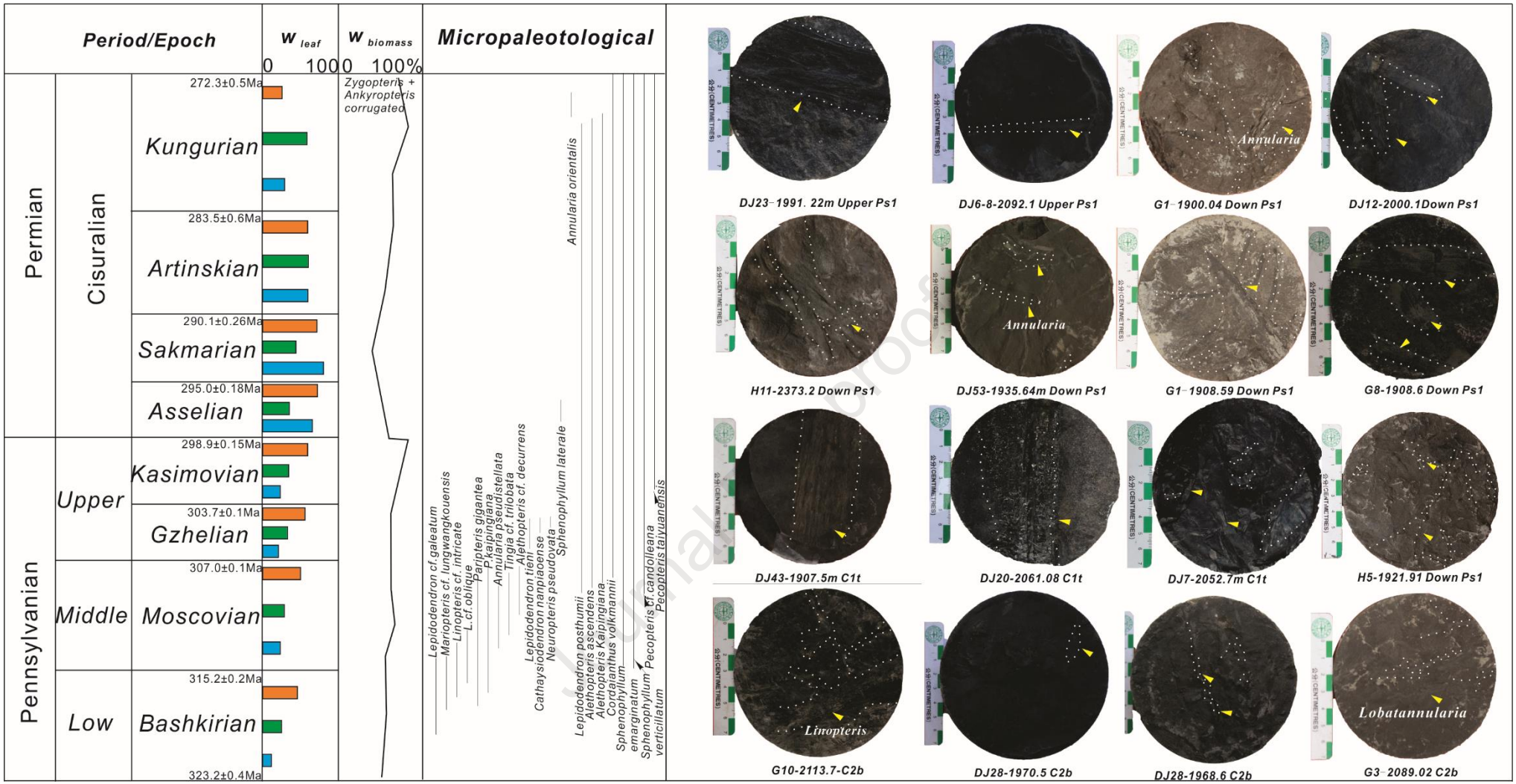
Period/Epoch
W_{leaf}
$W_{biomass}$
Micropaleotological
0 1000 0 100%
Permian
Pennsylvanian
Cisuralian
Upper
Middle
Low
272.3±0.5Ma
Kungurian
283.5±0.6Ma
Artinskian
290.1±0.26Ma
Sakmarian
295.0±0.18Ma
Asselian
298.9±0.15Ma
Kasimovian
303.7±0.1Ma
Gzhelian
307.0±0.1Ma
Moscovian
315.2±0.2Ma
Bashkirian
323.2±0.4Ma
Zygopteris + Ankyropteris corrugated
Annularia orientalis
Lepidodendron cf.galeatum
Mariopteris cf. lungwangkouensis
Linopteris cf. intricate
L.cf.oblique
Paripteris gigantea
P.kaipingiana
Annularia pseudistellata
Tingia cf. trilobata
Alethopteris cf. decurrens
Lepidodendron tieni
Cathaysiodendron nanpiaoense
Neuropteris pseudovata
Sphenophyllum laterale
Lepidodendron posthumii
Alethopteris ascendens
Alethopteris Kaipingiana
Cordaianthus volkmannii
Sphenophyllum emarginatum
Sphenophyllum verticillatum
Pecopteris cf. candolleana
Pecopteris taiyuanensis
Root fossil
Stem fossil
Leaf fossil
DJ23-1991. 22m Upper Ps1
DJ6-8-2092.1 Upper Ps1
Annularia
G1-1900.04 Down Ps1
DJ12-2000.1Down Ps1
H11-2373.2 Down Ps1
Annularia
DJ53-1935.64m Down Ps1
G1-1908.59 Down Ps1
G8-1908.6 Down Ps1
DJ43-1907.5m C1t
DJ20-2061.08 C1t
DJ7-2052.7m C1t
H5-1921.91 Down Ps1
Linopteris
G10-2113.7-C2b
DJ28-1970.5 C2b
DJ28-1968.6 C2b
Lobatannularia
G3-2089.02 C2b

FIG 15

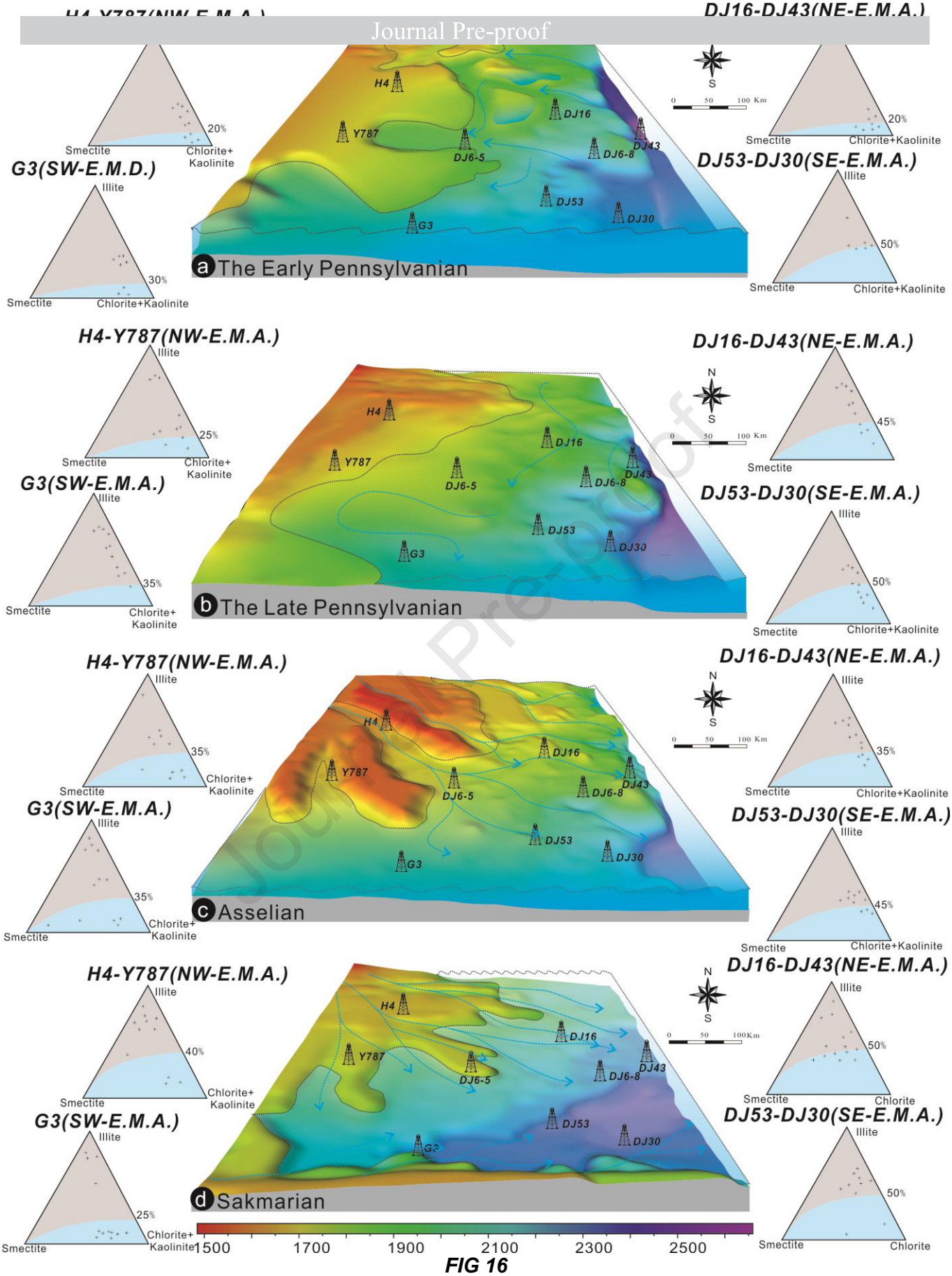

FIG 16

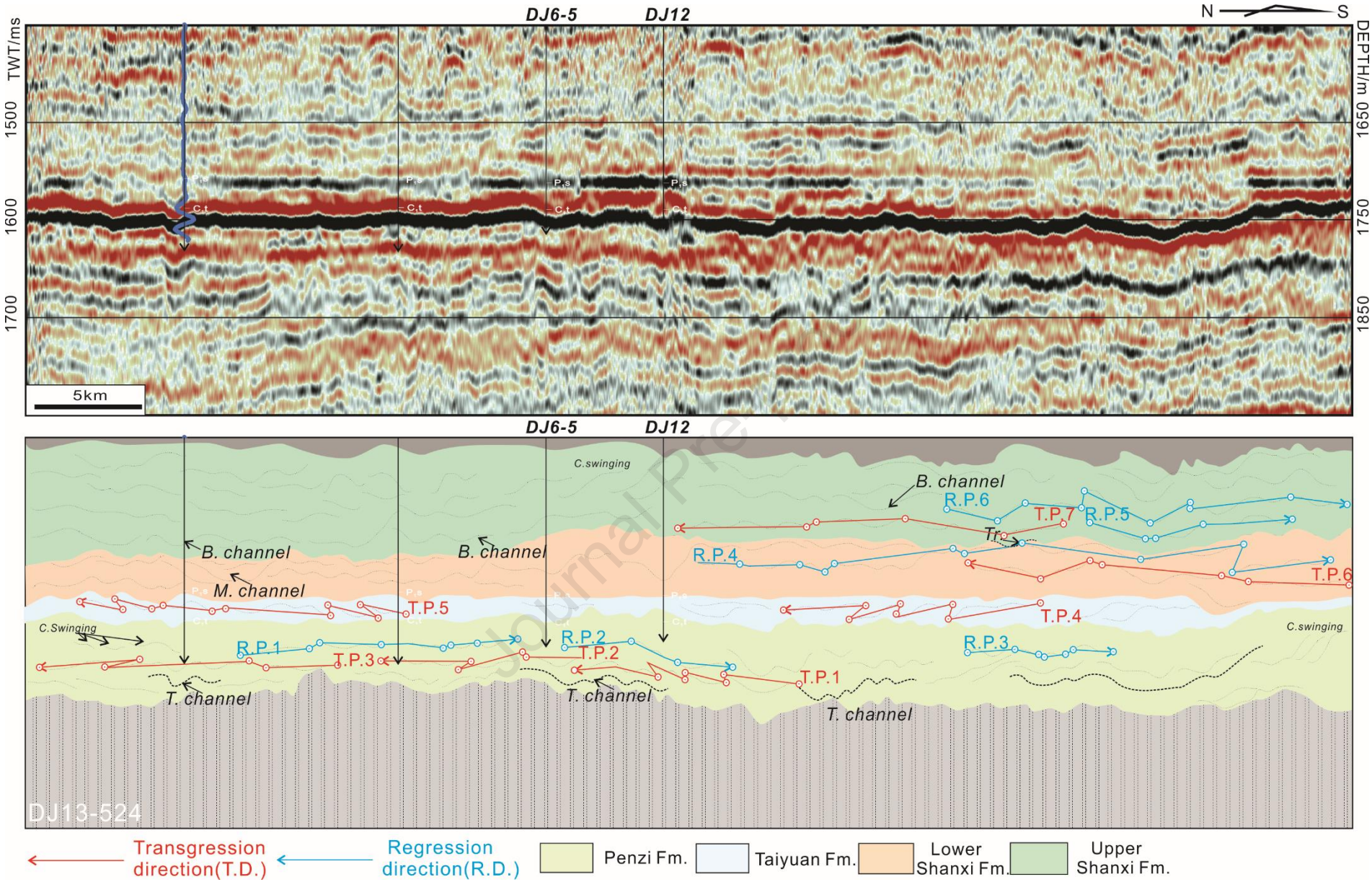

FIG 17

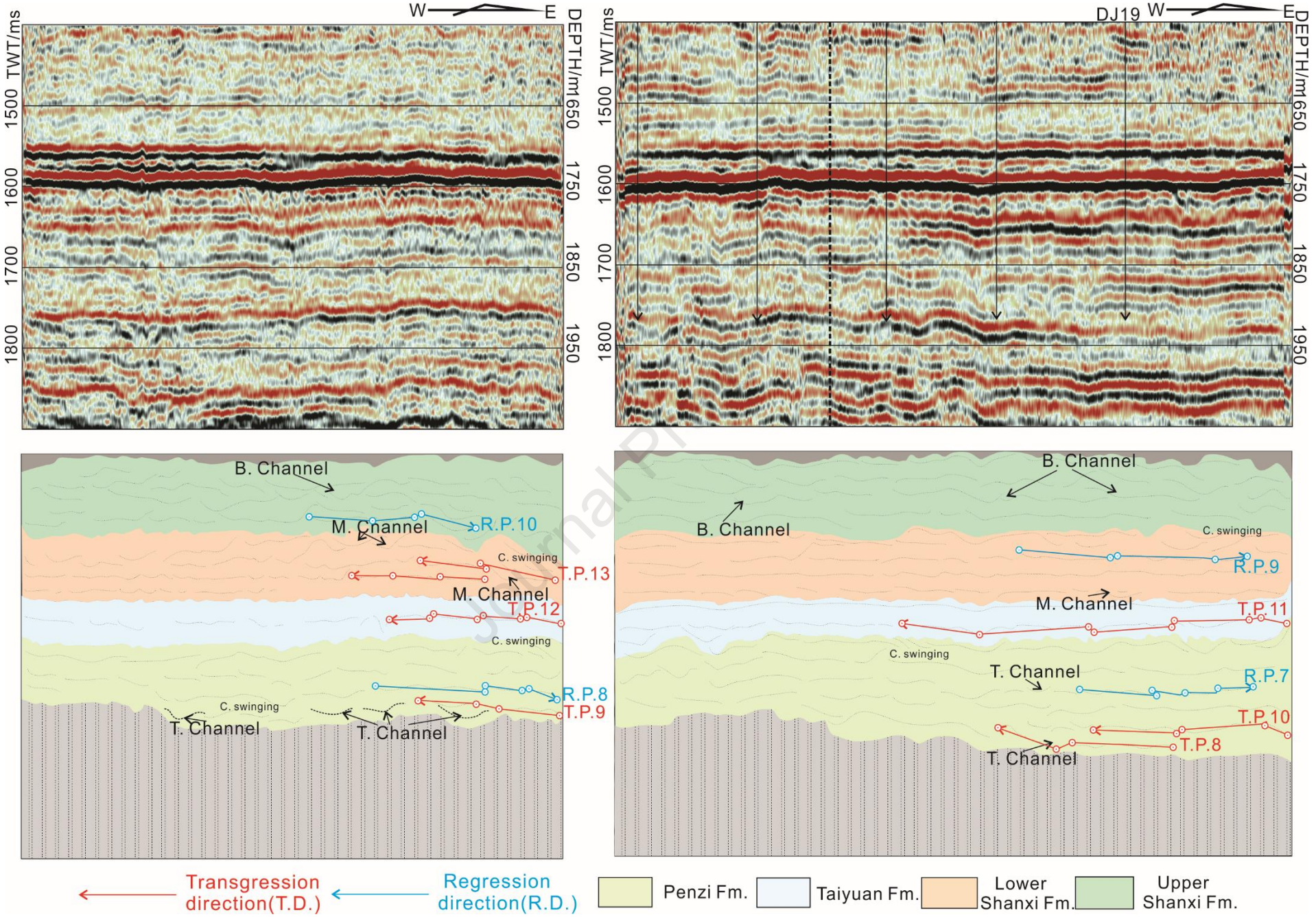
W
E
TWT/ms
DEPTH/m
1500
1600
1700
1800
1650
1750
1850
1950
DJ19
B. Channel
M. Channel
R.P.10
C. swinging
T.P.13
T.P.12
R.P.8
T.P.9
T. Channel
R.P.9
T.P.11
R.P.7
T.P.10
T.P.8
Transgression direction(T.D.)
Regression direction(R.D.)
Penzi Fm.
Taiyuan Fm.
Lower Shanxi Fm.
Upper Shanxi Fm.

FIG 18

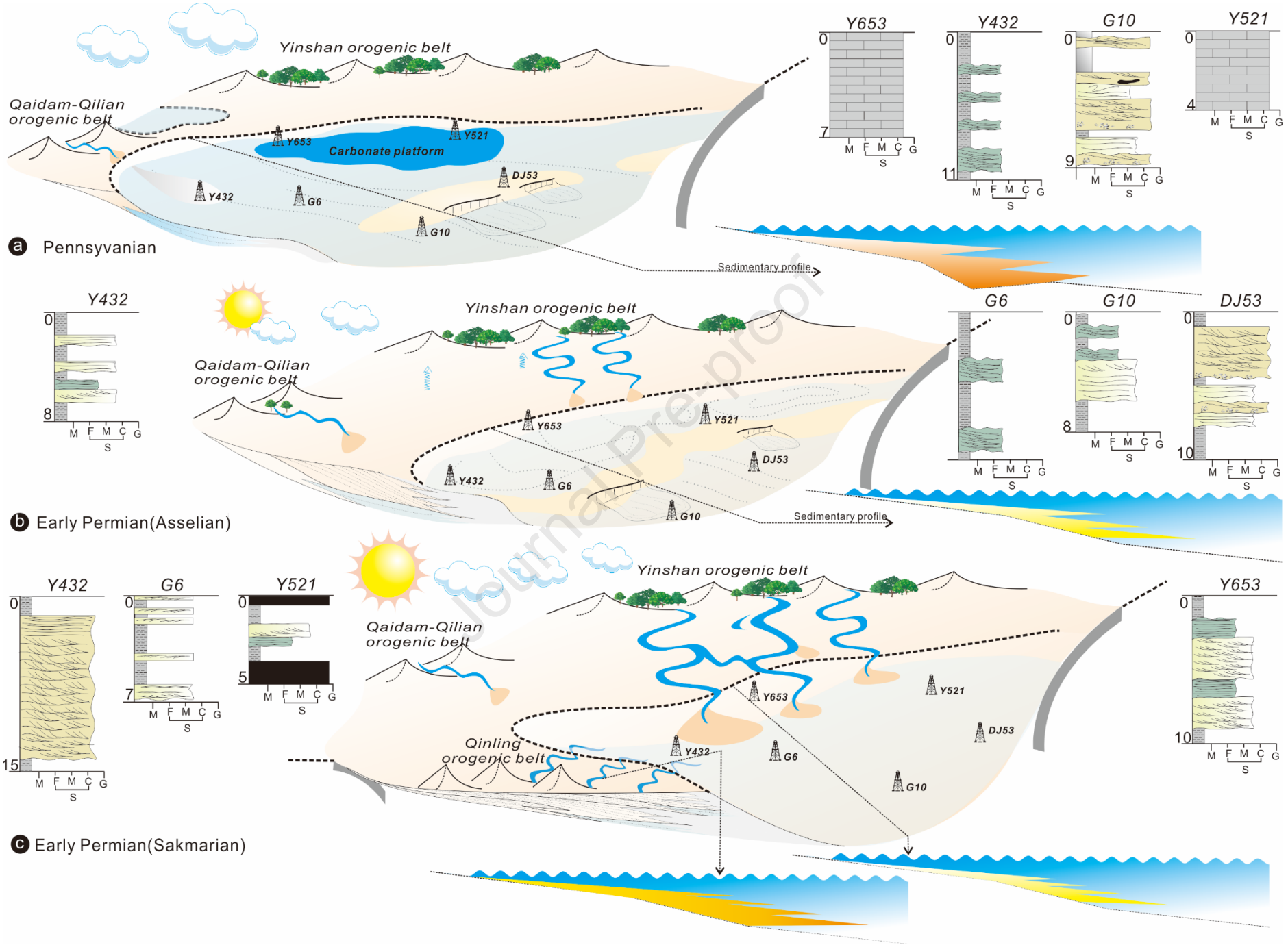

FIG 19

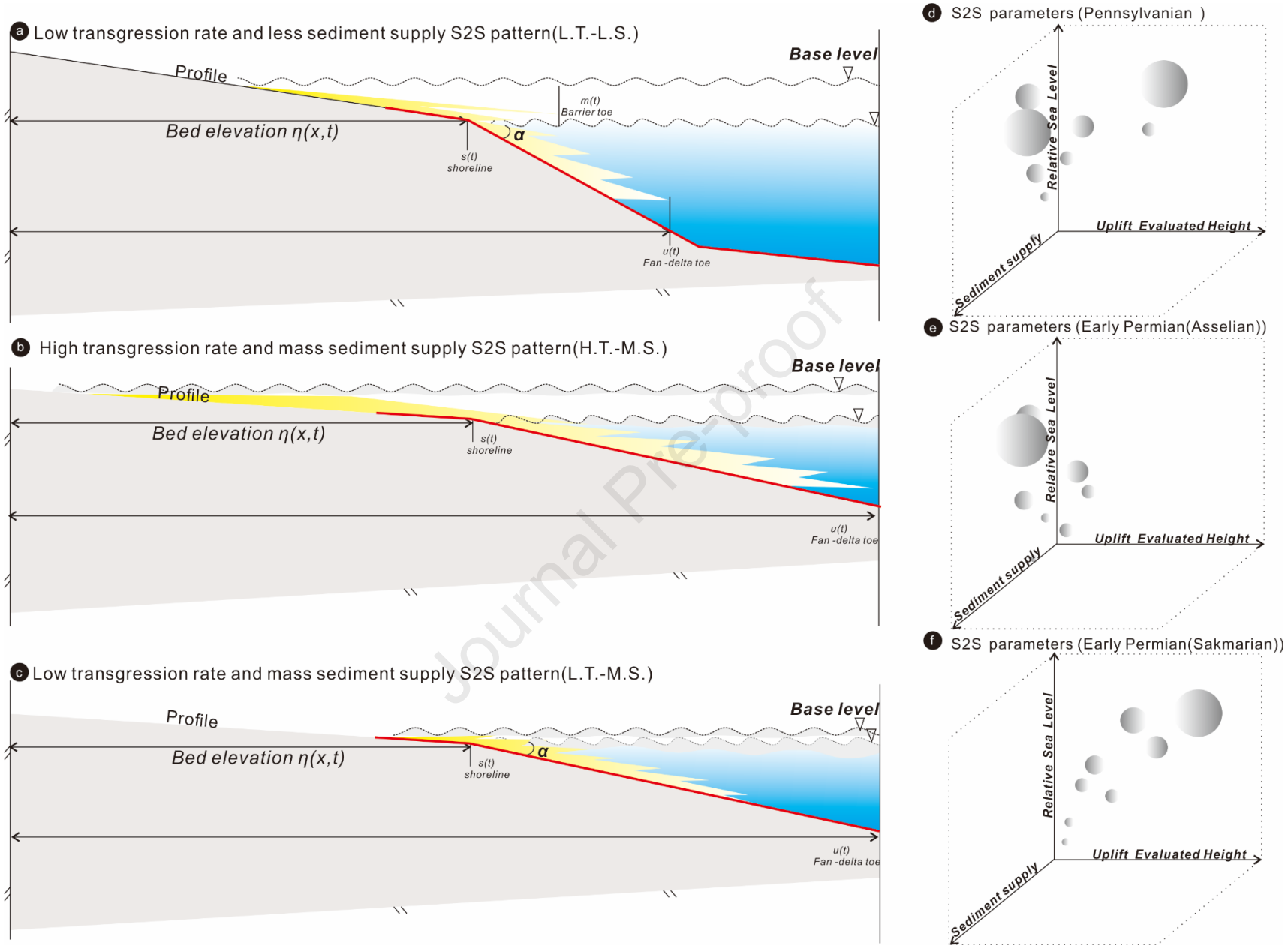

FIG 20

Highlight

1. Identified provenance area of the eastern margin of the Ordos Basin transfer from the Qaidam–Qilian orogenic belt to multiprovenance areas during the Pennsylvanian the late Carboniferous–early Permian.

2. Reconstructed the clockwise evolution process of the paleo sea level in the eastern margin of the Ordos Basin during the Paleozoic

3. Identified different types of source-to-sink systems insight from the spatial discrepancy of the sea level and sediment supply.

4. Proposed a integrated method to determine the dominating factors influencing the transgression/regression process

Declaration of interests

☒ The authors declare that they have no known competing financial interests or personal relationships that could have appeared to influence the work reported in this paper.

☐The authors declare the following financial interests/personal relationships which may be considered as potential competing interests: